Numerical Analysis of Multiphase Flow in Bubble Columns and Applications for Microbial Fuel Cells

Robert Picardi

Thesis submitted to the faculty of the Virginia Polytechnic Institute and State University in

partial fulfillment of the requirements for the degree of

Master of Science

In

Mechanical Engineering

Francine Battaglia

Jason He

Scott Huxtable

April 7, 2015

Blacksburg, VA

Numerical Analysis of Multiphase Flow in Bubble Columns and Applications for Microbial Fuel Cells

Robert Picardi

ABSTRACT

Computational fluid dynamics (CFD) modeling was used to predict the hydrodynamics of a column reactor. Bubble columns have applications across many engineering disciplines and improved modeling techniques help to increase the accuracy of numerical predictions. An Eulerian-Eulerian multi-fluid model was used to simulate fluidization and to capture the complex physics associated therewith. The commercial code ANSYS Fluent was used to study two-dimensional gas-liquid bubble columns. A comprehensive parameter study, including a detailed investigation of grid resolution was performed. Specific attention was paid to the bubble diameter, as it was shown to be related to cell size have significant effects on the characteristics of the flow. The parameters used to compare the two-dimensional (2D) cases to experimental results of Rampure, et. al. were then applied to a three-dimensional (3D) geometry. It was demonstrated that the increase in accuracy from 2D to 3D is negligible compared to the increase in CPU required to simulate the entire 3D domain. Additionally, the reaction chamber of a microbial fuel cell (MFC) was modeled and a preliminary parameter study investigating inlet velocity, temperature, and acetate concentration was conducted. MFCs are used in wastewater treatment and have the potential to treat water while simultaneously harvesting electricity. The spiral spacer and chemical reactions were modeled in a 3D geometry, and it was determined that inlet velocity was the most influential parameter that was simulated. There were also significant differences between the 2D and 3D geometries used to predict the MFC hydrodynamics.

Acknowledgements

There are a great deal of people to whom I owe gratitude for successful completion of my Master's degree. To begin, I would like to thank my graduate advisor, Dr. Francine Battaglia, for her guidance, support, and expertise in the subject of Computational Fluid Dynamics. I would like to thank Dr. Jason He for providing me the opportunity to work with his team on the study of microbial fuel cells and for providing the impetus for this research. I would also like to thank Dr. Scott Huxtable for being willing to serve alongside Dr. Battaglia and Dr. He as part of my committee. I also thank my fellow graduate students in the CREST lab for helping when I encountered obstacles and always taking the time to give helpful feedback. Finally, I must thank my wife, Kelly, and the rest of my family, who encouraged me to return to school and supported me whole-heartedly over the last two years.

Table of Contents

List of Figures

List of Tables

Nomenclature

A	Area
A_f	Pre-Exponential Factor
a	Under-relaxation factor
b	Temperature Exponent
C	Hypotenuse
C_A	Concentration of Acetate
C_D	Coefficient of Drag
d_b	Bubble Diameter
E_r	Activation Energy
e_a	Approximate Relative Error
$\vec{F}$	Force
f	Drag Function
G	Turbulent Kinetic Energy
h	Representative grid size
K	Interphase Momentum Exchange Coefficient
k	Covariance
k_r	Reaction Rate Constant
N	Total number of cells
R	Universal gas constant
r	refinement factor
Re	Reynolds Number
r	Refinement Factor
T	Temperature
S	One Dimensional Control Volume
U_p	Phase Weighted Velocity

V	Volume
$\vec{v}$	Velocity
α	Volume Fraction
Γ	Surface Area to Volume Ratio
$\Delta x, y$	Length of change in specified direction
ε	Dissipation Rate
θ	General Variable
λ	Bulk Viscosity
μ	Mixture Viscosity
Π	Turbulence Source Term
ρ	Density
$\hat{\rho}$	Effective Density
ρ_{rq}	Phase Reference Density
$\bar{\bar{\tau}}$	Stress Tensor
χ	Node value
∇	Gradient
$\emptyset$	Convected Variable

Subscripts/Superscripts

i	Unspecified number in a defined range
p, q	Unspecified phases
M	Unspecified number of phases

Chapter 1. Introduction

1.1.   Purpose and Applications

Microbial fuel cells (MFCs) have two important purposes, water treatment and harvesting electricity. An MFC gets its name from the culture of micro-organisms that live inside the reaction chamber, where the treatment and harvesting take place. As the untreated water is pumped through the chamber, it interacts with the culture, which begins to feed on the impurities and treat the water. A byproduct of the reaction is free electrons, which are collected by a copper wire on which all the micro-organisms live. By this process, two objectives are achieved, treated water and collection of energy [1]. Currently, the energy gains from MFCs are minimal, but the hope is to understand more about the fluid flow through the reaction chamber so that certain aspects can be optimized to enhance the reaction to hasten both the treatment and energy harvesting processes [2].

Primarily, MFCs are used in waste-water treatment plants. The nature of the process lends itself very clearly to this application; however, understanding the physics could provide applications beyond just water treatment facilities. The MFC can very easily be applied in any situation where certain chemical reactions occur on large scales. Chemical plants could see significant energy gains if this technology were to develop. Also, understanding the flow through the MFC geometry could aid in the production of other such materials of similar structure. There is significant research being performed on tube flow in the presence of twisted tapes [3]. These tapes are very similar to the spacer geometry presented in the MFC, and they are widely used for nuclear power stations and many other heat exchanging devices [3].

In addition to the microbial fuel cell applications, this study also serves to further the understanding of multiphase flow in bubble columns. Bubble columns are a widely studied topic in the field of fluid dynamics and have a wide array of applications from nuclear energy production [4] to inducing chemical reactions [5]. Understanding better models for bubble columns can help eliminate the need for tedious and expensive experiments and allow for accurate representations of these complex multiphase systems. In this study, bubble columns are simulated in three-dimensions (3D), and the prior studies of Law [6-7] are extended. Case studies are performed using particular parameters that have deepened the understanding of modeling bubble columns, which will serve to help future research in this field approximate results with increased accuracy.

1.2. Objectives

The main objective of the present work is to use the commercial CFD code ANSYS Fluent v14.5/15 to model and simulate the fluid flow through the reaction chamber of an MFC. It is further desired to use these results to provide the VT Civil Engineering team information about the important characteristics of the flow that effect the reaction between the micro-organisms and the impurities in the water. From the objectives outlined herein, the intended purpose of the present work will enhance the understanding of using Fluent to model flow through an MFC. In addition, this study is to increase the understanding of modeling bubble columns and shed light on the importance of particular parameters in the calculations. The knowledge gained will allow for a higher level of study in the realm of multiphase bubble column simulations.

1.3.   Literature Review

In order to verify results and build the most robust models to simulate the systems being tested, a substantial literature review is required. Because of the interdisciplinary nature of this work, the literature review spanned beyond simply the computational realm and touched on work in various fields of study.

1.3.1. Bubble Column Experiments

In an effort to properly model bubble column flows, the experimental work performed by Rampure et al. [8] and Mudde et al. [9] was reviewed. The geometry and initial conditions used in the 2D simulations are all derived from these papers, and it is their experimental work that is used to validate the models used to simulate multiphase flow. Multiphase flow is governed by the same conservation equations that dictate the physics of single-phase flow. The difference is that there are now two phases with separate densities, viscosities, and many other characteristics which are now interacting. In the case of bubble columns, air is introduced in the form of bubbles at the base of a channel containing water. The air moves up through the region of water and breaches the surface, where it is free to exit the channel through an outlet at the top. The interaction between the two phases while the air is mixed with the water in the lower region of the channel is an interesting phenomenon because of the physics of mixing.

The experimental work presented in the papers written by Rampure et al. and Mudde et al. allowed for verification of the models run in two dimensions. This experimental data and literature are crucial in developing a model and setting boundary and initial conditions. Using information such as mean bubble diameter and inlet velocity provided a guide for the selection of models. Throughout this document, these papers will be referenced to justify the selection of various conditions, parameters, and settings.

1.3.2. Bubble Column Computations

Deify Law wrote several papers on the use of CFD to analyze bubble column flow [6-7]. He even compared his numerical work to experimental data of Rampure et al. [8] and Mudde et al [9]. While reviewing his results, it was determined that he too had noticed an adverse relationship between fine grid resolutions and gas holdup profiles at specific channel heights. This study will be explained in further detail in Chapter 3 of this thesis. Law's paper also helped to explain the theory behind some of the discretization methods and parameters used to simulate the flow. Many figures will be presented later in this study, but in order to introduce the system being tested and provide preliminary visualization, time-averaged contours of volume fraction are presented in Figure 1.1 for a simulation of a bubble column. The blue represents water and the red represents air. Lighter shades of blue and green represent bubbles forming and ascending in the column. Having this visual representation should complement other quantitative data that will be shown as profiles in the following sections and chapters.
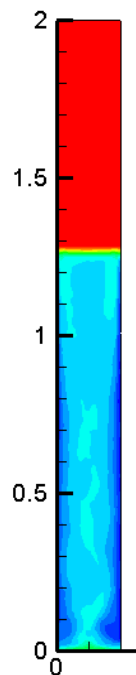
Figure 1.1: Time-averaged contours of air volume fraction for the 2D bubble column.

4

1.3.3. Grid Convergence Index and Bubble Diameter Studies

Recorded in this thesis are two case studies that are performed to model and simulate bubble columns. The first is a test of grid resolution on convergence, and a standard practice of a Grid Convergence Index (GCI) calculation is performed. This method is adopted directly from a paper written by Celik et al [10]. This paper provides step-by-step instructions describing the process of performing a GCI study. These procedures are performed in both the 2D and 3D studies that are executed in this study, and the detailed results will be discussed in Sections 3.3.1.2 and 3.4.3.

Additionally, a study on the effect of bubble diameter and grid convergence is investigated. There are no similar papers to be found on this subject, so it was decided that the discoveries of this study should be documented and published. This process has been initiated, and hopefully the product will be a journal publication in the near future. While no similar papers were discovered, there are papers that discussed bubble diameter and appropriate size selections. Rampure et al. [8] and Mudde et al. [9] discuss the use of high-speed cameras to observe the mean bubble sizes in their experiments. A paper by Lage and Espósito provides a more detailed range of mean bubble sizes measured in different bubble columns [11]. Also, some papers have been published discussing similar topics in gas-solid flows [12, 13], and one written by Monahan et al. [14] was found to be particularly useful. The thesis by Allison Studley [15], provides helpful information related to flow regimes and characterization based on the geometry and initial conditions.

1.3.4. Microbial Fuel Cell and Chemical Reaction Documentation

Many papers were recommended by the VT team of Civil Engineers working on the MFC project. These papers included the description of the chemical reactions, geometry, and auxiliary settings. They also provided a more holistic understanding of MFCs, and presented justification for their importance and applications in the real world. A paper by Logan et al. provided a comprehensive overview of the functionality of MFCs and the chemical reactions that drive the system [16]. Picioreanu et al. [17] provided a numerical model-based perspective on MFCs in a journal paper written in the field of Bioelectrochemistry. This paper served as a great reference and is the most similar to the work being performed in this study. The final paper in this area of the research that is used heavily was written by Ge et al. [18]. This paper described the geometry of the particular type of fuel cell being modeled and included more helpful information on their effectiveness to treat waste water.

1.4.   Outline of the Thesis

Chapter 2 presents the methodology behind modeling multiphase flow the governing equations and numerical approaches employed by Fluent. Chapter 3 details the background of multiphase flow specific to an investigation of bubble columns. This chapter provides a detailed inspection of important parameters and how they affect simulation results. Specifically, grid resolution and bubble diameter studies are highlighted. This chapter presents results using both two-dimensional (2D) and 3D simulations. Chapter 4 examines the design of the MFC geometry, the introduction of chemical reactions to the system, and the results of a preliminary parameter study. Finally, Chapter 5 includes a summary of the contributions made, recommendations for future work, and a conclusion of the study.

Chapter 2. Methodology

The multiphase flow theory of the commercial code ANSYS Fluent v14.5 is discussed in this chapter [19-20]. The computational code is combined with the foundation of fluid dynamics that drives all decisions that were made with respect to models and parameters [21]. The theory will be broken into sections consisting of governing equations, numerical approach, and initial and boundary conditions.

2.1.   Governing Equations

An Eulerian-Eulerian multiphase flow model is chosen to simulate flow in a bubble column. The Eulerian-Eulerian model represents each phase as interpenetrating continua, where each phase is separate, yet interacting, and the volume of a phase cannot be occupied by another phase. The assumption of interpenetrating continua introduces the concept of phasic volume fractions, whereby the sum of the fraction of space occupied by each of the phases equals one. The phasic volume fraction equation is given by:

$$V_q = \int_V \alpha_q dV \tag{2.1}$$

and

$$\sum_{q=1}^{n} \alpha_q = 1 \tag{2.2}$$

where V represents the volume of each phase, n represents the total number of phases, and α denotes the volume fraction of each phase. Clearly, the sum of all the volume fractions must equal one. The two considered are the liquid water phase, which is the primary phase, and the gas phase, which is the secondary phase. Volume fraction of the gas phase is commonly referred to as the gas holdup.   Although simple, this equation is an important one throughout the

calculations made to ensure continuity and conservation of energy. The effective density of each phase is given by:

$$\hat{\rho}_q = \alpha_q \rho_q \qquad (2.3)$$

where ρ is the physical density of each phase. The Eulerian-Eulerian model allows for incorporation of multiple secondary phases.

The laws of conservation of mass and momentum are satisfied, respectively, by each phase. Thus, the Eulerian-Eulerian model solves a set of momentum and continuity equations simultaneously, causing it to be one of the most involved of the multiphase models available.

2.1.1. Conservation of Mass

Conservation of mass is one of the fundamental equations of all fluid dynamics. The continuity equation for a phase is:

$$\frac{1}{\rho_{rq}}\left(\frac{\partial}{\partial t}\left(\alpha_q \rho_q\right) + \nabla \cdot \left(\alpha_q \rho_q \vec{v}_p\right) = \sum_{p=1}^{n}\left(\dot{m}_{pq} - \dot{m}_{qp}\right)\right) \qquad (2.4)$$

where ρ_{rq} represents the phase reference density, $\vec{v}_p$ is the velocity of a particular phase, and $\dot{m}_{pq}$ represents mass transfer between phases. In the case of this open system, no mass transfer occurs between phases; however, mass transfer will become an important factor between species when chemical reactions are modeled in the MFC simulations. Because there is no mass transfer in the bubble column reactor, the terms on the right hand side of the equation can be omitted, reducing the continuity equation to:

$$\frac{1}{\rho_{rq}}\left(\frac{\partial}{\partial t}\left(\alpha_q \rho_q\right) + \nabla \cdot \left(\alpha_q \rho_q \vec{v}_p\right) = 0\right) \qquad (2.5)$$

This simple equation is used for all continuity calculations.

2.1.2. Conservation of Momentum

The equation of momentum for fluid-fluid multiphase interactions in the Eulerian model can be expressed as:

$$\frac{\partial}{\partial t}\left(\alpha_q \rho_q \vec{v}_p\right) + \nabla \cdot \left(\alpha_q \rho_q \vec{v}_p \vec{v}_p\right) = -\alpha_q \nabla \rho + \nabla \cdot \bar{\bar{\tau}}_q + \alpha_q \rho_q \vec{g}$$

$$+ \sum_{p=1}^{n}\left(K_{pq}\left(\vec{v}_p - \vec{v}_q\right) + \dot{m}_{pq}\vec{v}_{pq} - \dot{m}_{qp}\vec{v}_{qp}\right) + \left(\vec{F}_q + \vec{F}_{lift,q} + \vec{F}_{vm,q} + \vec{F}_{wl,q} + \vec{F}_{td,q}\right)$$

(2.6)

Equation 2.6 incorporates the sum of all different forces on the flow. The term $\bar{\bar{\tau}}$ is the stress tensor, K is the interphase momentum exchange coefficient, $\vec{F}_q$ is an external body force, $\vec{F}_{lift,q}$ is a lift force, $\vec{F}_{vm,q}$ is a virtual mass force, $\vec{F}_{wl,q}$ is a wall lubrication force, and $\vec{F}_{td,q}$ is a turbulent dispersion force. Several of these terms are dropped when assessing the particular flow of interest, namely: virtual mass, wall lubrication, and turbulent dispersion.

The left hand side of Equation 2.6 represents the acceleration components of the system. The first term represents the unsteady acceleration and the second term represents the convective acceleration of the flow. The first term on the right hand side of Equation 2.6 takes the pressure changes into account for all phases in the system. The second term is a stress-strain tensor term, represented by:

$$\bar{\bar{\tau}}_q = \alpha_q \mu_q\left(\nabla \vec{v}_q + \nabla \vec{v}_q^T\right) + \alpha_q \left(\lambda_q - \frac{2}{3}\mu_q\right)\nabla \cdot \vec{v}_q \bar{\bar{I}}$$

(2.7)

where μ_q and λ_q are the shear and bulk viscosity of gas phase q, $\vec{v}_q^T$ is the transpose of the velocity gradient, and $\bar{\bar{I}}$ is the identity matrix. Since the velocity gradient term is equal to zero for incompressible flow, the simplified stress-strain tensor term for this particular case can be written:

$$\bar{\bar{\tau}}_q = \alpha_q \mu_q \left(\nabla \vec{v}_q + \nabla \vec{v}_q^T \right) \tag{2.8}$$

The third term on the right hand side of Equation 2.6 provides the effects of gravitational force on the flow. The fourth group of terms inside the summation includes an interaction force between gas and liquid phases as well as terms representing mass transfer between phases. The fifth and final grouping of terms includes the additional forces previously mentioned. Taking into account which terms can be neglected, the momentum equation for the gas phase can be simplified to the following form:

$$\frac{\partial}{\partial t} \left(\alpha_q \rho_q \vec{v}_p \right) + \nabla \cdot \left(\alpha_q \rho_q \vec{v}_p \vec{v}_p \right) = -\alpha_q \nabla \rho + \nabla \cdot \bar{\bar{\tau}}_q + \alpha_q \rho_q \vec{g}$$
$$+ \sum_{p=1}^{n} \left(K_{pq} (\vec{v}_p - \vec{v}_q) \right) + \left(\vec{F}_q + \vec{F}_{lift,q} \right) \tag{2.9}$$

Equation 2.9 represents the complete, simplified expression for conservation of momentum.

2.1.2.1. Gas-Liquid Interaction

An interfacial area exists between two phases in a mixture, and is important in predicting transfers between phases. The formulation used to express this area numerically is an algebraic method that takes advantage of the fact that the sum of all volume fractions must equal 1, and thus the values are inversely related. The model is derived from the surface area to volume ratio, Γ_p, which is shown in Equation 2.10 for the spherical air bubbles being considered:

$$\Gamma_i = \frac{6\alpha_p (1 - \alpha_p)}{d_p} \tag{2.10}$$

Here, d_p is the bubble diameter. The complementary volume fraction term, α_p, is introduced to guarantee that the interfacial area concentration approaches 0 as α_p approaches 1.

2.1.2.2. Drag Coefficient Model - Schiller-Naumann

In any dynamic interaction between two distinct fluid phases, there will be drag present. There are many different models available to simulate drag in a multi-fluid flow, but all calculations for the case at hand utilize the Schiller-Naumann model. This selection is the default model to account for drag forces in fluid-fluid flows and is applicable and accurate in most flow regimes. Since this simulation does not present any particularly special characteristics (i.e. large bubble variation), it is accepted as the most appropriate for the flow conditions at hand. The drag function, f, used in the Schiller-Naumann model is:

$$f = \frac{C_D Re}{24} \tag{2.11}$$

where C_D is the coefficient of drag and Re is the Reynolds number. The coefficient of drag is determined by:

$$C_D = \begin{cases} 24(1 + 0.15Re^{0.687})/Re, & Re \leq 1000 \\ 0.44, & Re > 1000 \end{cases} \tag{2.12}$$

The Reynolds number is calculated by:

$$Re = \frac{\rho_q |\vec{v}_p - \vec{v}_q| d_b}{\mu_q} \tag{2.13}$$

Equations 2.11 to 2.13 provide a complete description of how the drag in the system is calculated. Since it was determined that drag will have meaningful effects on the system due to the differences in the phases present, it is included in all simulations.

2.1.3. Turbulence Model

The flows being modeled in this study typically do not exist in a purely laminar region. There are elements of turbulence induced by the inlet velocities, the geometry of the channel, and the interaction of the phases.

2.1.3.1. Dispersed $k - \varepsilon$ Turbulence Model

It was determined that the most appropriate turbulence model for the flows observed in these cases is the $k - \varepsilon$ turbulence model. Within this model, there are three options for the turbulence multiphase model, dispersed, mixture, or per phase. The dispersed model is chosen since the water is the continuous phase in this system, and air represents a dilute secondary phase. The turbulence in the continuous phase, which is water, is determined by the following equations. The Reynolds stress tensor is formulated by:

$$\bar{\bar{\tau}}''_q = -\frac{2}{3}\left(\rho_q k_q + \rho_q v_{t,q} \nabla \cdot \vec{U}_q\right) + \rho_q v_{t,q}\left(\nabla \vec{U}_q + \nabla \vec{U}_q^T\right) \tag{2.14}$$

where $\vec{U}_q$ is the phase-weighted velocity. The turbulent viscosity of phase q can be expressed as:

$$\mu_{t,q} = \rho_q C_\mu \frac{k^2_q}{\varepsilon_q} \tag{2.15}$$

where ε_q is the dissipation rate and C_μ is a constant set to 0.09. The characteristic time of the turbulent eddies can similarly be written:

$$\tau_{t,q} = \frac{3}{2} C_\mu \frac{k_q}{\varepsilon_q} \tag{2.16}$$

Likewise, the turbulent eddies length scale can be defined as:

$$L_{t,q} = \sqrt{\frac{3}{2}} C_\mu \frac{k^{3/2}_q}{\varepsilon_q} \tag{2.17}$$

With these definitions, the transport equations can now be introduced:

$$\frac{\partial}{\partial t}\left(\alpha_q \rho_q k_q\right) + \nabla \cdot \left(\alpha_q \rho_q \vec{U}_q k_q\right) = \nabla \cdot \left(\alpha_q \frac{\mu_{t,q}}{\sigma_k} k_q\right) + \alpha_q G_{k,q} - \alpha_q \rho_q \varepsilon_q + \alpha_q \rho_q \Pi_{k_q} \tag{2.18}$$

$$\frac{\partial}{\partial t}\left(\alpha_q \rho_q \varepsilon_q\right) + \nabla \cdot \left(\alpha_q \rho_q \vec{U}_q \varepsilon_q\right)$$

$$= \nabla \cdot \left(\alpha_q \frac{\mu_{t,q}}{\sigma_\varepsilon} \varepsilon_q\right) + \alpha_q \frac{\varepsilon_q}{k_q}\left(C_{1\varepsilon} G_{k,q} - C_{2\varepsilon} \rho_q \varepsilon_q\right) + \alpha_q \rho_q \Pi_{\varepsilon_q} \tag{2.19}$$

where $G_{k,q}$ is the turbulent kinetic energy and Π_{k_q} and Π_{ε_q} are source terms used to model the influences of the two phases. These two equations neglect buoyancy, user-defined source terms, and dilation.

2.1.3.2. Turbulence Interaction

Turbulence interaction includes the influence of the dispersed phase on the multiphase turbulence equations. The Simonin et al. [19] model includes turbulence interaction by adding source terms to the turbulence transport equations. The equations linking the interaction between discrete and continuous phases in the turbulence interaction model are:

$$\Pi_{k_q} = \sum_{p=1}^{M} \frac{K_{pq}}{\alpha_q \rho_q} X_{pq}(k_{pq} - 2k_q + \vec{v}_{pq} \cdot \vec{v}_{dr}) \tag{2.20}$$

$$\Pi_{\varepsilon_q} = 1.2 \frac{\varepsilon_q}{k_q} \Pi_{k_q} \tag{2.21}$$

Here, Π_{k_q} and Π_{ε_q} are the source terms that appear in Equations 2.18 and 2.19 earlier. Equation 2.20 links the turbulence interaction model to the $k - \varepsilon$ turbulence model. k_{pq} is the covariance

in the velocities and $\vec{v}_{pq}$ and $\vec{v}_{dr}$ are the relative and drift velocities, respectively. X_{pq} can be described by:

$$X_{pq} = \frac{\rho_p}{\rho_p + C_{VM}\rho_p} \tag{2.22}$$

In general, for dispersed flows, $X_{pq} \sim 1$. Using Equation 2.22 in conjunction with the overall turbulence model equations, the turbulence of the entire system can be simulated.

2.2. Numerical Approach

Conservation of mass and momentum are solved by Fluent with integral equations. A finite volume method approach is adopted for local satisfaction of the governing equations. An additional benefit of this methodology is that it can solve these equations while allowing for relatively coarse grid resolutions.

2.2.1. Pressure-Based Solver Algorithm

A pressure based solver utilizes the theories of continuity and conservation of momentum to determine the velocity field. The velocity field is corrected by the pressure field and must satisfy Equation 2.4. The Navier-Stokes equations must be solved iteratively until the solution converges.

The pressure based solver segregates the phasic momentum, shared pressure, and phasic volume fraction equations in order to solve them separately. The phase-coupled semi-implicit method for pressure linked equations (PC-SIMPLE) algorithm is chosen as it is an extension of the SIMPLE algorithm and developed expressly for multiphase flow applications. In the PC-SIMPLE method, velocities are solved coupled by phases, and then a block algebraic multigrid

scheme is employed to solve the vector equation representing all the velocity components of the phases simultaneously.

2.2.2. Spatial Discretization

Ideally, spatial discretization schemes should effectively translate the data stored at cell centers into values that represent entire faces. The approach employs second-order upwind schemes, and these are most important for both momentum and volume fraction discretization. For the momentum equations, the quadratic upwind interpolation for convective kinematics (QUICK) was determined to be the most suitable scheme, and the modified high resolution interface capturing (HRIC) scheme was selected for volume fractions.

2.2.2.1. QUICK Method

The QUICK scheme is most useful in computing a high-order value of the convected variable, Ø . The scheme uses a weighted-average of both second-order-upwind and cell-centered interpolations of the convected variable. A diagram of this discretization method can be seen in Figure 2.1, where P is the node of interest, and E and W are the nodes east and west of the cell center .
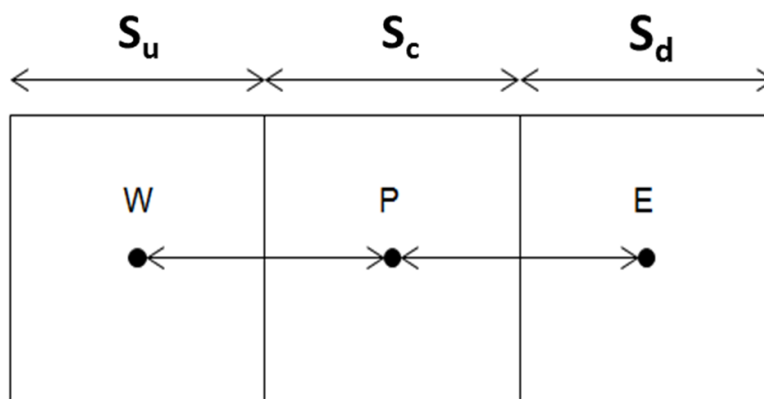
Figure 2.1: One-dimensional control volume used in the QUICK scheme for solving the momentum equations in spatial discretization [19].

Here, the three sections, S_u, S_c, and S_d, refer to the upwind, cell-centered, and downwind sections of the control volume. If it is assumed that the flow moves from left to right across the control volume divided into three sections of length S_u, S_c, and S_d, then the convected variable can be calculated as follows:

$$\emptyset_e = \theta \left[\frac{S_d}{S_c + S_d} \emptyset_P + \frac{S_c}{S_c + S_d} \emptyset_E \right] + (1 - \theta) \left[\frac{S_u + 2S_c}{S_u + S_c} \emptyset_P - \frac{S_c}{S_u + S_c} \emptyset_W \right] \qquad (2.23)$$

The parameters $\emptyset_W$, $\emptyset_P$, and $\emptyset_E$ represent the cell centered values for the upwind, local, and downwind of the convected variable. The θ term determines from which direction the convected variable will be calculated. If $\theta = 1$, then the QUICK method will employ a downwind scheme, and if $\theta = 0$, then an upwind scheme will be employed. The following work assumes $\theta = 0$, and thus is an upwind discretization method.

2.2.2.2. Modified HRIC Method

The HRIC method utilizes a combination of upwind and downwind differencing to determine discrete values of volume fraction. This method is most suitable for multiphase flow, for which a purely upwind differencing scheme results in non-physical values. To understand the formulation of this scheme, it is necessary to consider three adjacent cells, labeled W, P, and E from left to right. For visualization, please refer to Figure 2.1. E is the acceptor cell, P is the donor cell, and W is the upwind cell. To find the normalized cell value of volume fraction, $\widetilde{\emptyset}_c$:

$$\widetilde{\emptyset}_c = \frac{\emptyset_P - \emptyset_W}{\emptyset_E + \emptyset_W} \qquad (2.24)$$

The normalized face value, $\widetilde{\varnothing}_f$, can be solved using:

$$\widetilde{\varnothing}_f = \begin{cases} \widetilde{\varnothing}_c, & \widetilde{\varnothing}_c < 0 \ \text{or} \ \widetilde{\varnothing}_c > 1 \\ 2\widetilde{\varnothing}_c, & 0 \leq \widetilde{\varnothing}_c \leq 0.5 \\ 1, & 0.5 \leq \widetilde{\varnothing}_c \leq 1 \end{cases} \tag{2.25}$$

Fluent then switches to the one-dimensional, bounded version of the QUICK scheme based on the angle between the face normal and interface normal, as is demonstrated by the following.

$$\varnothing_f^{\widetilde{U}Q} = \begin{cases} \widetilde{\varnothing}_c, & \widetilde{\varnothing}_c < 0 \ \text{or} \ \widetilde{\varnothing}_c > 1 \\ MIN(\widetilde{\varnothing}_f, \dfrac{6\widetilde{\varnothing}_c + 3}{8}), & 0 \leq \widetilde{\varnothing}_c \leq 1 \end{cases} \tag{2.26}$$

where $\varnothing_f^{\widetilde{U}Q}$ is the value as a product of this modified version of the QUICK scheme.

This yields a corrected face volume fraction value, $\widetilde{\varnothing}_f^*$:

$$\widetilde{\varnothing}_f^* = \widetilde{\varnothing}_f \sqrt{\cos\Theta} + (1 - \sqrt{\cos\Theta}) \, \varnothing_f^{\widetilde{U}Q} \tag{2.27}$$

where

$$\cos\Theta = \frac{\nabla\varnothing \cdot \vec{d}}{|\nabla\varnothing||\vec{d}|} \tag{2.28}$$

The face volume fraction can be obtained by:

$$\varnothing_f = \widetilde{\varnothing}_f^*(\varnothing_A - \varnothing_U) + \varnothing_U \tag{2.29}$$

This method proved to be particularly important in achieving physical results in 2D simulations. More details will be provided in the following chapter.

2.2.2.3. Green-Gauss Node-Based Method

Gradients are necessary to understanding several key aspects of the flow. They form secondary diffusion terms and velocity derivatives, thus enabling the discretization of the convection and diffusion terms of the conservation equations. The Green-Gauss node-based method computes the gradient discretization term by taking the arithmetic mean of the values of

all the nodes on a given face. When used to compute the gradient of a scalar at the cell center,

the Green-Gauss theorem takes on a discrete form and is expressed as:

$$(\nabla \emptyset)_{c0} = \frac{1}{v} \sum_f \overline{\overline{\emptyset}}_f \vec{A}_f \tag{2.30}$$

The face value, $\overline{\overline{\emptyset}}_f$, can also be expressed as the arithmetic mean of the node values on

the face, χ_f, and the expression is:

$$\overline{\overline{\emptyset}}_f = \frac{1}{\chi_f} \sum_n^{N_f} \overline{\overline{\emptyset}}_n \tag{2.31}$$

2.2.2.4. Under-Relaxation

Under-relaxation variables serve as solution inputs that help aid in convergence of the

simulation. Under-relaxation variables are important in pressure-based coupled systems to avoid

oscillatory convergence errors. Often, if too high or too low, these terms will either completely

damp the system and thus not allow for actual results, or they will be insufficient and will allow

for oscillatory errors to persist. Under-relaxation for each variable in the system can be

expressed as:

$$\emptyset = \emptyset_{old} + a\Delta\emptyset \tag{2.32}$$

and ensures that the new value depends on the value from the previous time-step, but with the

under-relaxation factor, a, scaling the change from one step to another.

Using the basic theory and formulations presented in this chapter, the work continues by

modeling bubble column flow. Various numerical models and techniques are tested and the

simulations will be validated with experimental data [8] in Chapter 3.

Chapter 3. Bubble Column Model

This chapter describes the elementary cases run in order to learn the basic principles of multiphase flow. It uses the experimental work of Rampure et al. [8] to validate a 2D model of a bubble column reactor.

3.1 Background

Multiphase flow in general behaves similar to simple single phase flow. It is still governed by the Navier-Stokes equations detailed in Chapter 2. These equations are modified to reflect the interaction of two separate phases, water and air, as described in Section 1.3.1. Instead of the flow being dominated by inertial forces, the viscous forces become increasingly important. In addition, the size of air bubbles in water and forces of drag become factors in the continuity of momentum equations, while turbulence forces and the effect of pressure on the flow take on an added level of complexity. These are the factors that separate multiphase flow from single phase cases.

3.1.1. Boundary Conditions

The bubble column reaction chamber being evaluated is a cylindrical configuration consisting of an inlet at its base, and outlet at the top, and walls surrounding it. In the simple 2D cases, this can be modeled as a rectangle to represent the vertical cross-section of the cylinder, with regions of both air and water initialized. As complexity increases, three dimensions are required, and the regions of air and water must be adjusted in order to reflect the true operating state of the fuel cell.   Air is introduced at the base, or "inlet" of the channel, and fluid is released from the top, or "outlet". A schematic of this geometry can be seen in Figure 3.1.
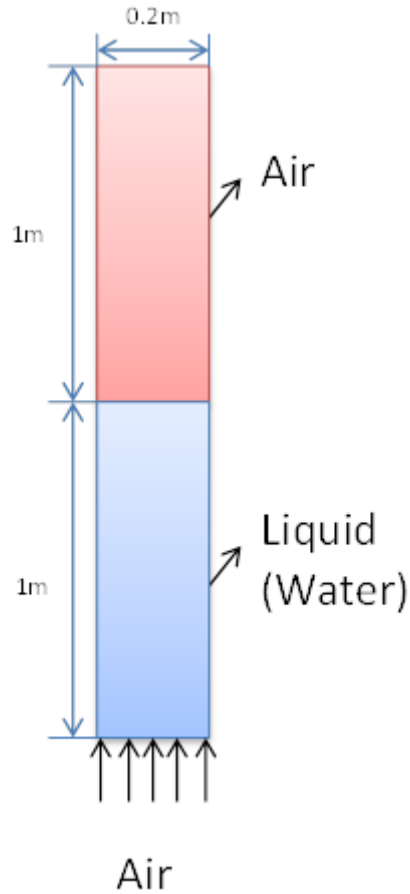
Figure 3.1: Schematic of the 2D geometry of the simple bubble column

In simple terms, the 2D analysis models a 3D bubble column. There have been significant studies of bubble columns in the past [8-9], but modeling them using CFD is not easy. To model the experiments of Rampure et al. [8], the walls are oriented in the vertical direction and are 2 meters long. The inlet, boundary, and outlet are evenly spaced at the bottom, middle, and top of the chamber, respectively. They are oriented horizontally and each has a length of 0.2 meters, as shown in Figure 3.1.

The walls have a no-slip boundary condition and serve to contain the fluids from spreading horizontally. The velocity inlet is at the bottom of the chamber, and is the face at which the air enters the reaction chamber at 0.1 m/s. Initially, water occupies the lower 1 m of

the channel and air occupies the upper regime. The boundary at the outlet is set to ambient pressure.

3.1.2. Initial Conditions

Initial conditions help to ensure convergence of the solution and that it accurately represents the physical system being modeled. There are two types of initial conditions which must be specified: air volume fraction in the reaction chamber, and y-velocity (vertical velocity) of the gas phase into the fluid region of the chamber. The volume fraction of air is based on experimental measurement provided by Rampure [8]. The inlet velocity is also based on the experiment in order to more accurately model the system.

3.1.3. Base Case Conditions

Throughout this chapter, studies will show the comparison between two parameters. For these studies to be effective, all other parameters in each case will be held constant in order to isolate the effects of an individual parameter. For this reason, a base case is established in order to have a standard to compare results. The settings of the base cases are summarized for reference. The base case does not employ virtual mass, neglected drift and surface tension, uses the Schiller-Naumann drag model, the dispersed $k - \varepsilon$ turbulence model with no turbulence specified at the boundaries, and is simulated with a bubble diameter of 0.005 m. In addition, the Green-Gauss node based spatial discretization and modified HRIC volume fraction discretization are employed, using a 30x300 grid resolution, and implicit, first-order time discretization. Finally, a time-step of 0.005 seconds is used, with 100 time-samples per second for time averaging and 50 iterations per time-step, and all residuals are required to converge to 10^{-4}.

3.2.   Physical Modeling

In this section, the details of the physical model used to simulate the preliminary 2D multiphase cases will be discussed. The important factors regarding parameters that were learned in the simple 2D simulations can be directly applied to the 3D case utilizing the MFC geometry.

3.2.1. Phase Interactions

A key factor in understanding multiphase flow is to learn more about the interaction of the different phases. Some of the more important parameters regarding the phase interaction are discussed in this section, notably virtual mass, lift, drag, and surface tension.

3.2.1.1. Virtual Mass

In many bubble column cases, virtual mass is a necessary force to be included in calculations. It is increasingly important when the density of the secondary phase is significantly smaller than that of the primary phase. This is the case here, as the density of air is much less than that of water. When virtual mass is included, the adverse and non-physical effects are very apparent in the results. The reasoning for the adverse effects is found in a paper by Monahan et. al. [14], which stated that for flows with column diameters exceeding 15 centimeters the virtual mass term can be neglected . Simulations are continued without virtual mass moving forward. In some instances, the presence of virtual mass actually caused the calculations to diverge, preventing any useful data from being gathered. The adverse effects of virtual mass can be observed in Figure 3.2, which shows air volume fraction profiles at two vertical cross-sections in the channel. The heights of these cross-sections, 0.15 m and 0.65 m, were chosen based on the experimental data available from Rampure et al. [8]. The solid circles represent the experimental data, and this notation will be consistent through the rest of the study. The solid blue line

represents the simulated results of the base case that has been previously described in Section 3.1.3, and the dashed red line represents the test case including the effects of virtual mass.
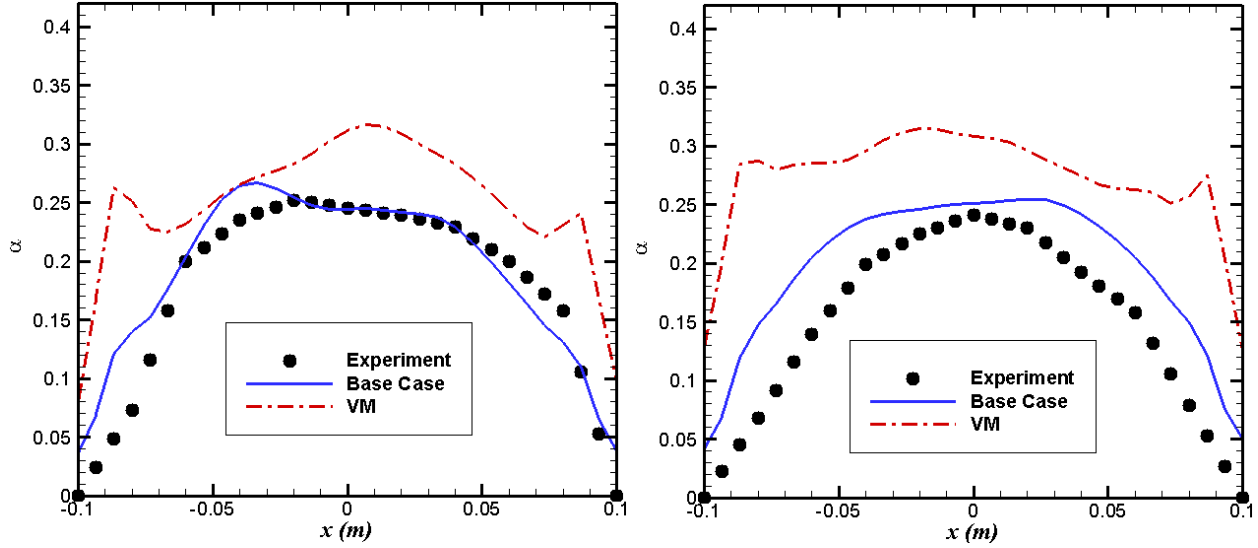
Figure 3.2: Air volume fraction profiles at (left) 0.15 m and (right) 0.65 m for cases testing effects of virtual mass.

3.2.1.2. Lift

When studying forces on moving systems, lift forces are evaluated to determine if they are significant. In most multiphase cases, lift forces are insignificant compared to drag and other forces, so inclusion is not necessary [22]. It only serves a meaningful purpose when there are large bubbles or particles present, but that is not the case with these simulations. Lift was further modeled, but it was determined that neglecting lift in these simulations would be the most effective way to capture the true effects of the flow [14].

3.2.1.3. Drag

Drag is often an important factor in fluid dynamics, and several different drag models were tested before it was decided that Schiller-Naumann model was ideal. The Schiller-Naumann model is applicable for all fluid-fluid multiphase interactions, which is exactly what

this case exhibits. Other models demonstrated stability issues, variable bubble size requirements, or were specifically designed for phenomena that are not being investigated.

3.2.1.4. Surface Tension

Surface tension is deemed to be an unimportant element in this case because of the inherent turbulent flow and thus very disjointed boundary between water and air phases. Also, due to the relatively coarse mesh in this simulation, the effects of surface tension are very minimal.

3.2.2. Turbulence

Another phenomenon for consideration is turbulence. Due to the velocities and viscosities of the materials in each phase, the Reynolds number of this flow is approximately 2000, and thus turbulence plays an important role in the simulations. The details of this role are discussed in the following sections.

3.2.2.1. Turbulence at the Boundaries

The turbulence at both the inlet and outlet of the reaction chamber are not well defined. Based on the initial conditions and geometry, there is no clear value for the turbulence in either location, so the decision was made to set the turbulence intensity to nearly 0 in order to reduce any unintentional effects of false turbulence at either boundary. The turbulence values would have been set to zero, but the solver would diverge, most likely due to division by zero.

3.2.2.2. Turbulence Model: Dispersed vs. Per Phase

There was some discussion over which turbulence model would be most appropriate for the bubble column. The dispersed model is designed to be used in flows with a dominant phase and one or more subordinate phases. The per phase model is designed for flows with two or

more equal phases. While the bubble column flow is initiated with two equal regions of separate phases, only air is introduced into the system, and the only interesting region of the flow is where bubbles move through water. Once the air bubble breaks at the surface of the water, the dynamics of the flow are no longer interesting in the context of this study. Therefore, water is treated as the primary phase, as it dominates the region of interest. Air is considered to be secondary, and a dispersed phase seemed most appropriate. To ensure this conclusion, cases were run with both dispersed and per phase models for turbulence. Interestingly, the results were nearly identical, but the dispersed model is chosen based on the logic stated previously and the fact that it is less computationally expensive and will thus get to the same answer more quickly.

3.2.3. Bubble Diameter

A bubble diameter of 0.005 m is chosen as the appropriate length for the simulations, as this is suggested by the experimental results of Rampure [8]. While this parameter seems fairly insignificant when first considered, it has actually been proven to be quite important. There is a direct connection between the bubble diameter, grid size, and the predictions from the simulations. This phenomenon is primarily a result of numerical stability limits, and thus will be discussed in more detail later in this chapter as part of the grid resolution summary (Section 3.3.1.3).

3.3.   Numerical Model

In CFD, the numerical modeling is critical for predicting accurate physics based on a set of discretized equations. This is where computational methods diverge from experimental methods in a very large way, and is one reason why accurate numerical models are necessary if the results are to be useful in real-world applications. The numerical calculations are separated into two different components of equal importance, space and time. The spatial and temporal

parameters must be well understood in order for the calculations to yield meaningful results. Discretization of these parameters will be described in the next section.

3.3.1. Spatial Formulations

Spatial discretization is essential for properly capturing the physical domain of an experiment. This section will detail the spatial discretization and grid resolution used to model the bubble column.

3.3.1.1. Discretization

Several different spatial gradient discretization methods were explored before the appropriate one was determined. The least-cells square based method makes assumptions that the solution is linear, and thus over-simplifies the calculations. The remaining options, the Green-Gauss node based and Green-Gauss cell based methods, are then compared. While very similar, the difference between these two methods is where the dependent variables are taken from and applied to. As their names suggest, one uses the node as the reference point, while the other uses the cell-center. In general, the node-based gradient is more accurate than the cell-based gradient, although it does require some additional computation time. After running simulations and realizing this additional time was minimal, it was determined that the Green-Gauss node based discretization method was most appropriate for multiphase flow.

Quite possibly the most important and least expected parameter investigated in this study is the volume fraction discretization. For quite some time, none of the calculations performed were providing sensible results, and the reason behind these problematic determinations was that the wrong volume fraction discretization method was being used. Originally, the QUICK method was being used, but when the modified HRIC method is utilized, the results become

much more realistic. The modified HRIC method incorporates a blend of upwind and downwind schemes, which provides more accuracy than QUICK, which is primarily an upwind scheme. This increased sophistication does require more computational time, but the improved predictions are very much worth the sacrifice. The QUICK method predicted non-parabolic profiles for volume fraction that would dip in the center of the column, which is known to be a non-physical result, as can be observed in Figure 3.3. The use of the modified HRIC method provided the expected parabolic profiles, thus validating the volume fraction discretization method. Although the QUICK method is generally useful and applicable for multiphase flow problems, the predictions of simulations showed that it is not appropriate for the bubble column model. For the remainder of the studies, the modified HRIC scheme will be used, and is incorporated into the base case model described in Section 3.1.3.
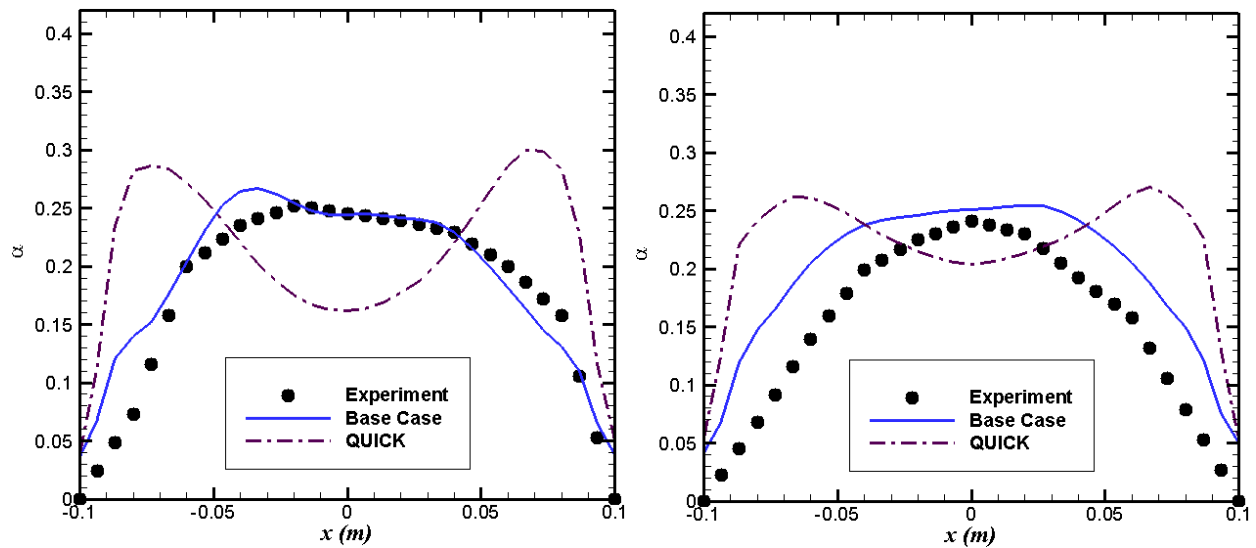
Figure 3.3: Air volume fraction profiles at (left) 0.15 m and (right) 0.65 m for cases testing effects of spatial discretization schemes.

3.3.1.2. Grid Resolution Study

Grid resolution studies are generally some of the most essential studies when determining the proper geometry and mesh for simulations. As discussed in Law et al. [8], a grid resolution study indicated that finer grid cells predicted poor results. The 30x300 grid resolution provided the most consistent and accurate data compared to the results of Rampure [8].
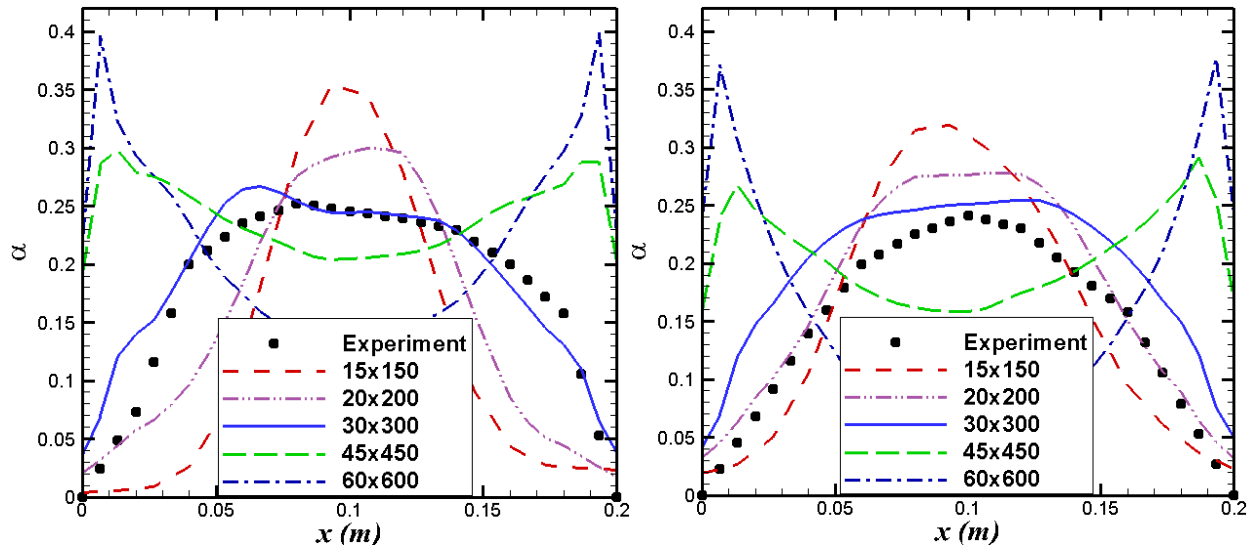
Figure 3.4: Air volume fraction profiles at (left) 0.15 m and (right) 0.65 m for cases testing effects of grid resolution.

The results of this grid resolution study are puzzling, as one would expect that finer grid resolution would always produce more accurate results. The reason that coarser grids are often chosen is that they are computationally less expensive, and have been shown to provide a sufficient level of accuracy. As shown in Figure 3.4, increasing grid resolution from 15x150 to 20x200, and then again to 30x300, the results improve notably with each grid refinement. Unexpectedly, the 30x300 case provides more accurate results than the finer grid resolutions explored. In fact, the 45x450 and 60x600 cases provide very non-physical results, with profiles that do not conform to the expected parabolic nature of bubble column flow.

A grid convergence index (GCI) study to assess the numerical uncertainty is performed using several grid resolutions, comparing the values of volume fraction at 31 different points across the bubble column [10]. Originally it was intended to use the 15x150, 30x300, and 60x600 grid resolutions in order to consistently double the grid size, a common technique in GCI studies. As can be seen in Figure 3.4, the 60x600 case provides completely non-physical results, and thus the data is not deemed worth incorporating in the study. Instead, a scaling factor of 1.5 is used, so the 20x200, 30x300, and 45x450 grid resolution cases are investigated. Special interest is shown to the 30x300 case, as these results have the best correlation to the experimental results that could be observed visually, and that is the motivation for this resolution being the medium grid size in the GCI study.

The calculation of the GCI begins by identifying the representative grid size h:

$$h = \left[\frac{1}{N} \sum_{i=1}^{N} (\Delta A_i) \right]^{\frac{1}{2}} \tag{3.1}$$

where ΔA_i is the area of the ith cell, and N is the total number of cells in the geometry. Next, the refinement factor, r, needs to be calculated:

$$r = \frac{h_{coarse}}{h_{fine}} \tag{3.2}$$

Here, r = 1.5 for both the coarse-medium and medium-fine comparisons. In an effort to find the apparent order, p, of the method:

$$p = \frac{1}{\ln(r)} \left| \ln \left| \frac{\alpha_3 - \alpha_2}{\alpha_2 - \alpha_1} \right| \right| \tag{3.3}$$

where the subscripted numbers refer to the fine (1), medium (2), and coarse (3) grid resolutions. Once the order is found for all data, the approximate relative error, e_a, can be found:

$$e_a^{21} = \left| \frac{\alpha_1 - \alpha_2}{\alpha_1} \right| \tag{3.4}$$

An equivalent calculation for medium-coarse approximate relative error is also made. Finally the GCI value can be calculated using the following equation:

$$GCI_{fine}^{21} = 0.625e_a^{21} \tag{3.5}$$

Likewise, the GCI_{coarse} can also be calculated [10]. Using this calculation technique, the results of the GCI study are summarized in Table 3.1.

Table 3.1: 2D GCI results for 20x200, 30x300, and 45x450 grids

y	Coarse/Medium	Medium/Fine
0.15 m	1.60%	1.17%
0.65 m	0.42%	0.75%

These results seem to be inconclusive at first. At the 0.15 m height in the column, the GCI study shows that the grids are converging as a finer grid size is used. This is the exact opposite of what the 0.65 m height results demonstrate. These conflicting results may be hard to interpret, but it is important to note that the percent differences between the coarse/medium and medium/fine results are small, less than 0.5% in both cases. What this means is that deviations from the medium grid case, in this situation the 30x300 resolution, do not provide significant improvements in accuracy of the results. Also, since one height is recommending a slightly finer grid and another recommending a slightly coarser grid, we can derive from these conflicting recommendations that the medium grid is quite close to the perfect grid selection. In fact, had these results not have been conflicting and both either recommended a coarser or finer grid, then this study would have shown that the 30x300 grid is not the ideal case, which would contradict

the results we have already observed. This supports the original claim that the 30x300 grid

resolution is the best grid to use for the current simulation.

3.3.1.3. Bubble Diameter Study

As previously discussed in this chapter, a bubble diameter of 0.005 m is modeled to

compare with experimental results [8]. It was observed that finer grid cells predicted non-

physical results, and the cell size is smaller than the bubble diameter. In fact, a 40x400 grid

resolution has a square grid with sides of length 0.5 cm, which is equivalent to the bubble

diameter. Referring to the results in Figure 3.4, it can be seen that all cases finer than this

threshold lose any physical volume fraction distribution, while all cases coarser than this show

the expected parabolic profiles.

This is an intriguing observation, and led to a formal bubble diameter study in which

many different bubble sizes and grid resolutions are tested to see if a relation could be observed

linking bubble diameter, grid size, and accurate results. It was hypothesized that the bubble

diameter should be one half of the diagonal of the grid size so that roughly two bubbles could fit

into each grid cell. This relation is the ratio of bubble diameter to grid size, which equals $1/\sqrt{2}$.

There are similar guidelines followed when simulating gas-solid flows, although these usually

recommend a particle diameter to grid size ratio of 1/10 [6]. Figure 3.5 depicts this theory,

where d_b is the bubble diameter, C is the hypotenuse, and $\Delta x = \Delta y = \Delta$, which is the grid cell side

length. In order to validate this hypothesis, many of the grid resolutions tested are intentionally

selected to test this theory. A table of all cases appears in Table 3.2. The rows italicized are the

ideal cases where $d_b/\Delta \approx 0.707$. The significant results of all these cases can be summarized in

Figure 3.6.

31
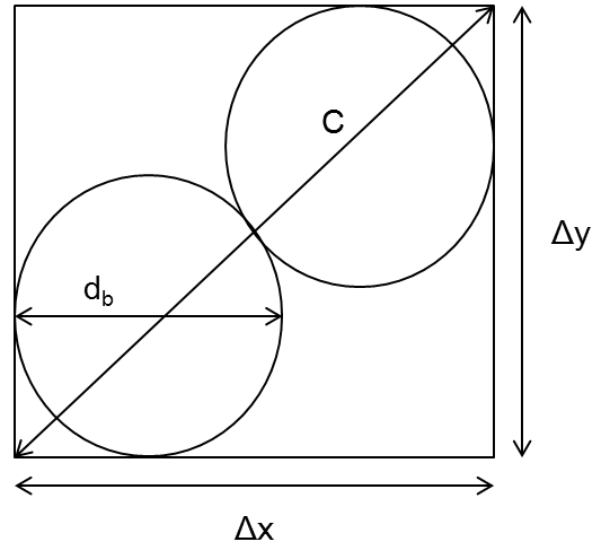
Figure 3.5: Visualization of one cell in the computational domain, depicting the ideal bubble diameter to grid size relationship.

From these results, it is concluded that the hypothesis held true. For the case with a bubble diameter of 0.5 cm, the ideal case (27x270) is clearly the most accurate compared to experimental data. Changing the grid resolution even slightly in either direction results in deviations from the experimental results. In the simulations with a bubble diameter of 0.35 cm, a 40x400 grid resolution is expected to yield the best results. While there is no experimental data available to validate the results with this bubble diameter, the 40x400 case results are the most uniform and parabolic of all grid resolutions. When the grid became too fine and the bubble diameter exceeded the cell size, as can be seen in the 60x600 and 80x800 cases, the "M" shaped profiles are observed again. Similarly, in the case with a bubble diameter of 0.2 cm, the ideal case (70x700) yields results that are most realistic. These results are not parabolic, as the flow has transitioned into a homogenous region with the smaller bubbles. Other grid resolutions with this bubble diameter predicted irregular profiles, and when the grid resolution is too fine, the beginning of the "M" shaped trend is identified.

Table 3.2: Summary of cases evaluated in the bubble diameter study. Ideal cases are in bold and italicized.

Grid Resolution	Δ (m)	d_b (m)	d_b/Δ	d_b/C
45x450	0.00444	0.0010	0.225	0.159
60x600	0.00333	0.0010	0.300	0.212
30x300	0.00667	0.0020	0.300	0.212
45x450	0.00444	0.0020	0.450	0.318
60x600	0.00333	0.0020	0.600	0.424
70x700	***0. 00286***	***0.0020***	***0.700***	***0.495***
100x1000	0.00200	0.0020	1.000	0.707
30x300	0.00667	0.0035	0.525	0.371
40x400	***0.00500***	***0.0035***	***0.700***	***0.495***
45x450	0.00444	0.0035	0.788	0.557
60x600	0.00333	0.0035	1.050	0.743
80x800	0.00250	0.0035	1.400	0.990
15x150	0.01333	0.005	0.375	0.266
20x200	0.01000	0.005	0.500	0.354
27x270	***0.00741***	***0.005***	***0.675***	***0.477***
30x300	0.00667	0.005	0.750	0.530
40x400	0.00500	0.005	1.000	0.707
45x450	0.00444	0.005	1.125	0.795
60x600	0.00333	0.005	1.500	1.060
15x150	0.01333	0.010	0.750	0.530
30x300	0.00667	0.010	1.500	1.060
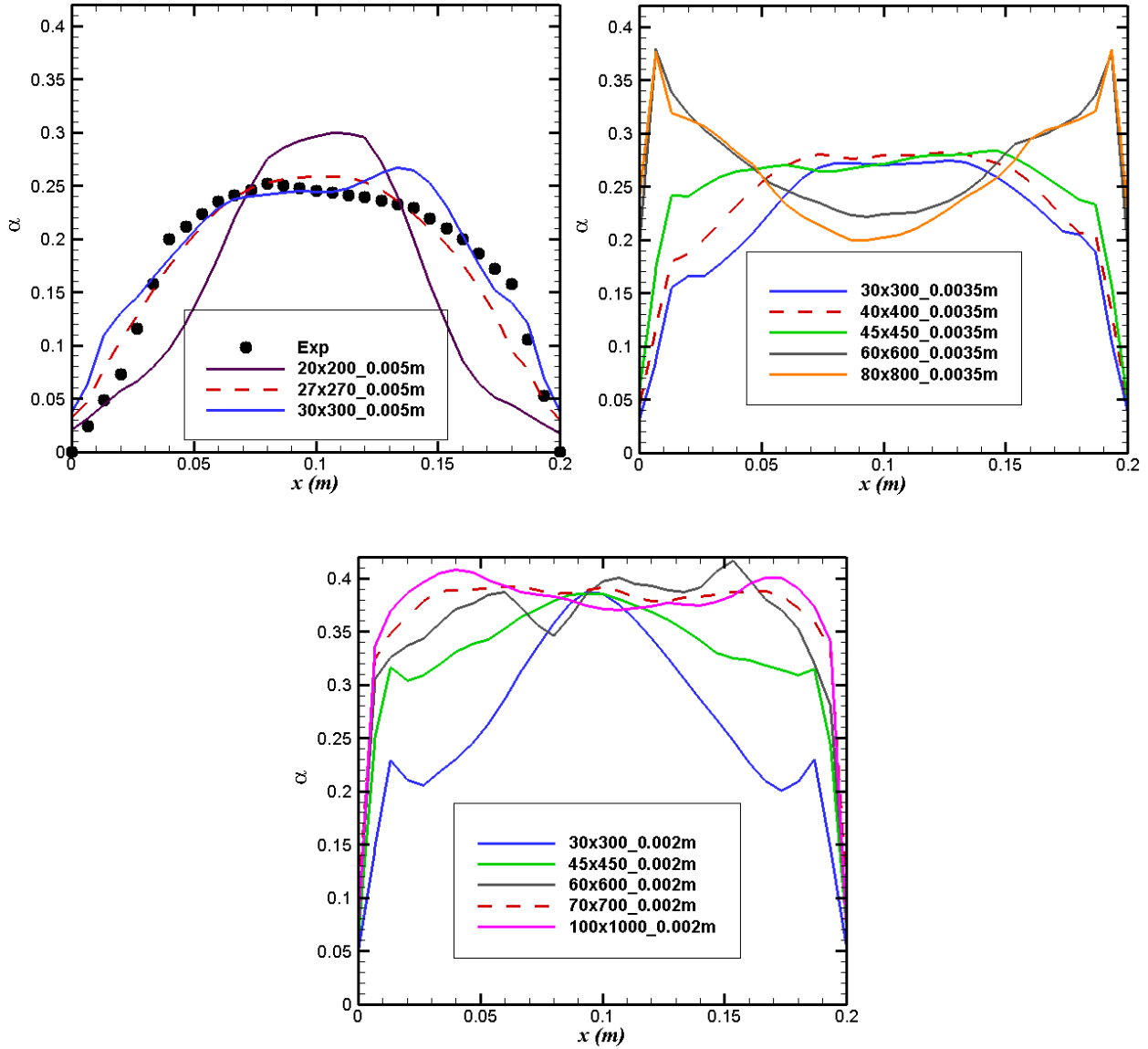
Figure 3.6: Air volume fraction results at different grid resolutions for bubble diameters of 0.5 cm (top left), 0.35 cm (top right), and 0.2 cm (bottom) at y = 0.15 m. The ideal case in each of these scenarios is denoted by the dashed red line.

Figure 3.7 provides instantaneous results comparing cases with different grid resolutions in order to develop a deeper understanding and visualization of the relationship between grid resolution and physical volume fraction. From these results, it is evident that finer grids have adverse impacts on bubble column predictions. Comparing the contours in Figure 3.7 to the profiles in Figure 3.4 provides a compelling depiction of the numerical errors produced by using

a mesh that is too fine when compared to the bubble diameter. Figure 3.7 (a) should be

compared to the red dashed line in Figure 3.4 representing the 15x150 resolution case. Likewise,

Figure 3.7 (b) should be compared to the blue solid line in Figure 3.4 representing the 30x300

resolution case, and Figure 3.7 (c) should be compared to the purple dashed line in Figure 3.4

representing the 60x600 resolution case. The 15x150 case (Figure 3.7 (a)) shows the volume

fraction of air highly concentrated in the center of the column. This is represented in Figure 3.4

by a tall and narrow parabolic peak that does not match the experimental data. The 60x600 case

(Figure 3.7 (c)) shows the volume fraction concentrating around the walls of the column, with

very little in the center of the geometry. This is represented in Figure 3.4 by an "M" shaped

profile, where the high regions of air are observed near the walls, with low regions in the center.

Finally, the 30x300 case (Figure 3.7 (b)) shows a natural distribution of air throughout the

column with a moderate concentration in the center and lower fractions of air near the walls.

The 30x300 prediction is the most true to the physics, and this is reflected in the parabolic

profiles in Figure 3.4 that closely match the experimental data.
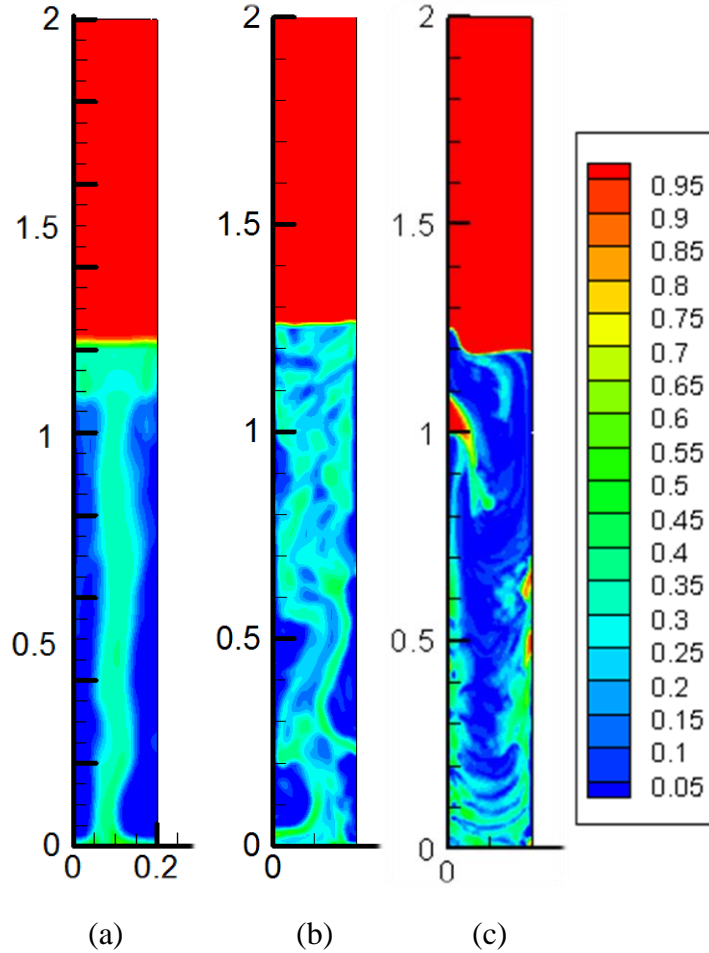
Figure 3.7: Instantaneous air volume fraction contours for grid resolutions of 15x150 (a), 30x300 (b) and 60x600 (c), with $d_b = 0.005$ m.

The bubble size directly affects the flow regime. When the bubbles are small, the flow is more homogeneous in nature, with a rather flat distribution of bubbles throughout the channel. When bubble sizes are larger, the flow becomes more heterogeneous in nature, and the air regions tend to gather in the middle of the column and ascend. Similarly, when the bubble diameter changes, altering the ratio of bubble diameter to grid size, the flow characteristics change also. Figure 3.8 provides instantaneous results, and it is evident that changing the bubble diameter changes the flow regime of the bubble column.
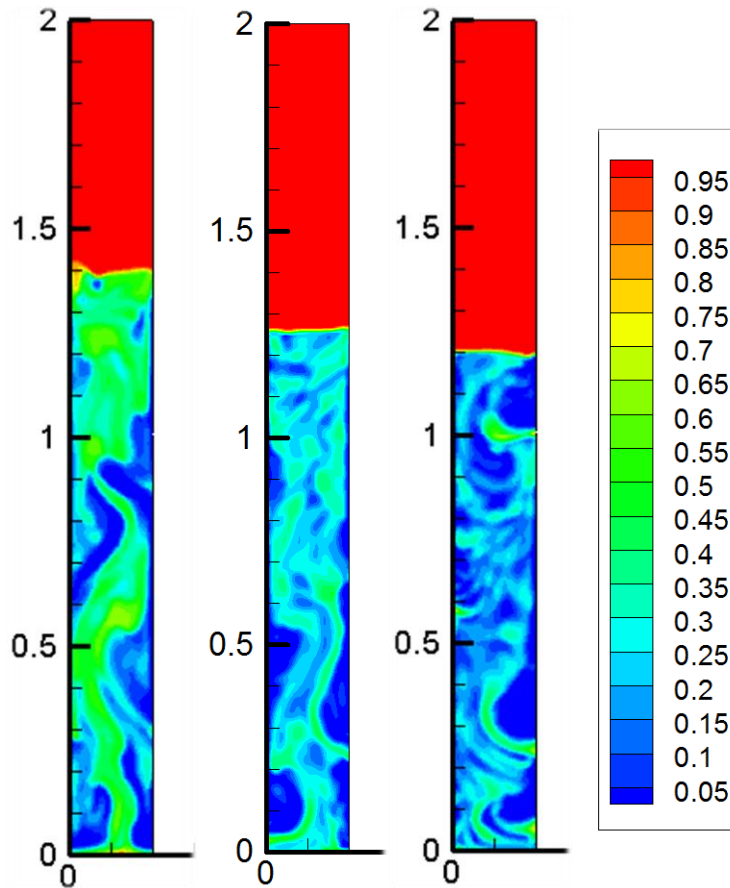
Figure 3.8: Instantaneous air volume fraction contours for bubble diameters of 0.2 cm (a), 0.5 cm (b), and 1 cm (c), with a 30x300 grid resolution.

Here, the results are slightly different from the varying grid resolution. The air volume fraction increases as the bubble diameter decreases, as is to be expected. Also, the smallest bubble diameter case has the highest density of bubbles in the middle of the column, while the largest bubble diameter case has a higher density along the walls. These distinctions can be explained by the fact that the flow is in a transitional region. In bubble column flows, the characterization of the flow is primarily determined by inlet velocity and channel diameter, and Figure 3.8 depicts this relationship.
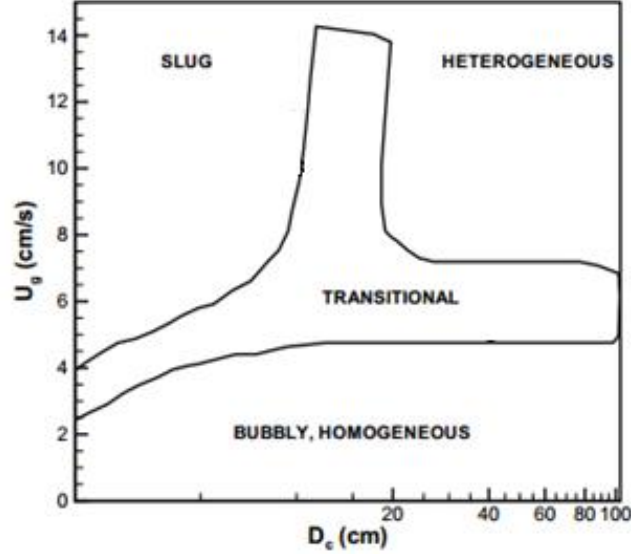
Figure 3.9: Bubble column flow regimes based on channel diameter and inlet velocity [15, 23].

Based on the channel diameter of 20 cm and inlet velocity of 10 cm/s, this flow exists in a transitional region; therefore, the overall characteristic can be easily influenced by rather small deviations, such as a change in bubble diameter. Because of this characterization, it is crucial when modeling bubble column simulations that exist in a transitional region to pay close attention to the bubble diameter selected. Choosing the wrong diameter could cause adverse effects on the results of the simulations.

3.3.2. Temporal Formulations

The second component of all the equations used in the calculations run in this case is time. Because this work is dynamic by nature, time plays a very important role in the calculations, and if the parameters are properly determined, the calculations will invariably diverge.

3.3.2.1. Implicit vs. Explicit Schemes

The implicit scheme is used exclusively in the simulations since it allows for larger ranges of time steps and does not introduce stability issues. Explicit methodology, while computationally less demanding, has very specific time step size requirements in order to avoid the instabilities that arise from the explicit finite difference analysis [24].

3.3.2.2. Transient Formulation

First-order implicit (FOI) formulas are used for their increased accuracy as well as decreased computation time. The alternative, the bounded second-order implicit (BSOI) formulas, were considered, but from results such as those presented in Figure 3.10, it is determined that they are not suitable for the simulations. Clearly, these results demonstrate the vast difference between first- and second-order methods. This variance is most noticeable at the 0.65 meter channel height, where completely non-physical results are predicted. Based on these results and numerous simulations, many which have not been presented, the FOI scheme is adopted as appropriate for all subsequent simulations.

Figure 3.10: Air volume fraction profiles at (left) 0.15 m and (right) 0.65 m for cases testing effects of transient formulation schemes.

3.3.2.3. Time Step and Courant–Friedrichs–Lewy Number

A rule of thumb is known as the Courant-Friedrichs-Lewy (CFL) condition. The CFL number is represented by the following equation:

$$CFL = \frac{v\Delta t}{\Delta x} \qquad (3.6)$$

In general, for single-phase flow, the CFL number should be approximately 1 and for multiphase flow, it should be approximately 0.2-0.3. Based on the results provided in this chapter, the ideal CFL number is actually much closer to 0.1. These results are supported by studies that claim that while there are standards that should be followed for multiphase flow, the CFL number should not determine the discretization but should be determined by observed convergence [25]. Since the velocity and mesh size are already determined, the time step uniquely determines the CFL number, so a time step study and CFL study are one in the same. For consistency purposes, all cases used the same time sampling rate of 100 time realizations per second, totaling 7000 realizations over the entire simulation. Figure 3.11 presents three CFL cases, and demonstrates that a time step size of 0.005 seconds, corresponding to a CFL of 0.075 is ideal for the simulations. From these profiles, it can be seen that at the 0.15 m height, all three CFL values yielded very similar results, with no one value standing out as clearly the most accurate. At the 0.65 m height, however, the CFL value of 0.075 provided slightly better results than the rest, and thus this is selected as the base value for future cases.
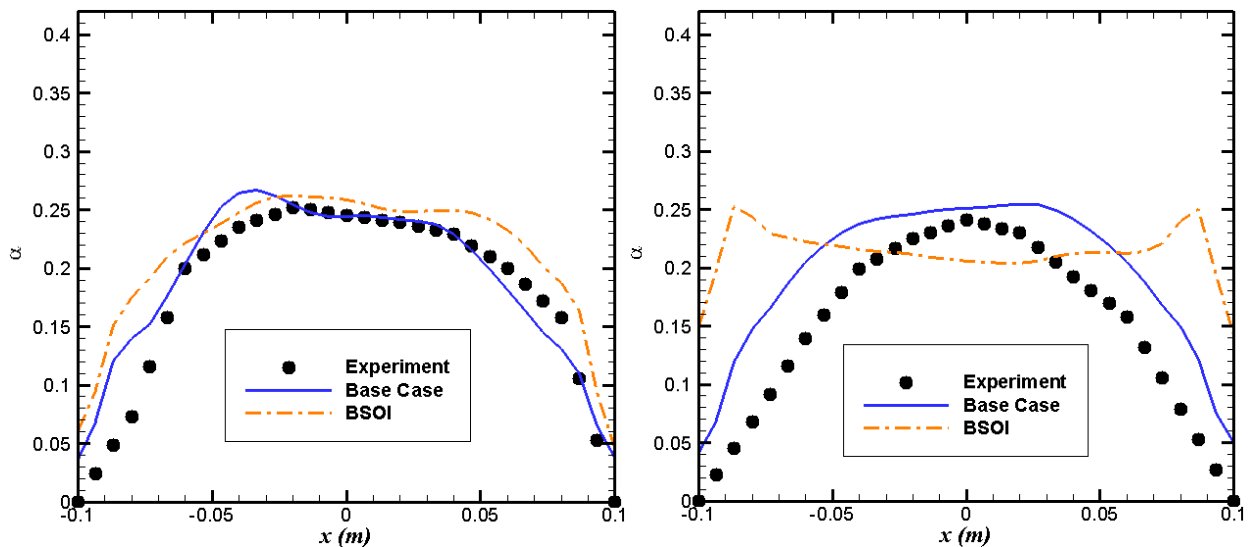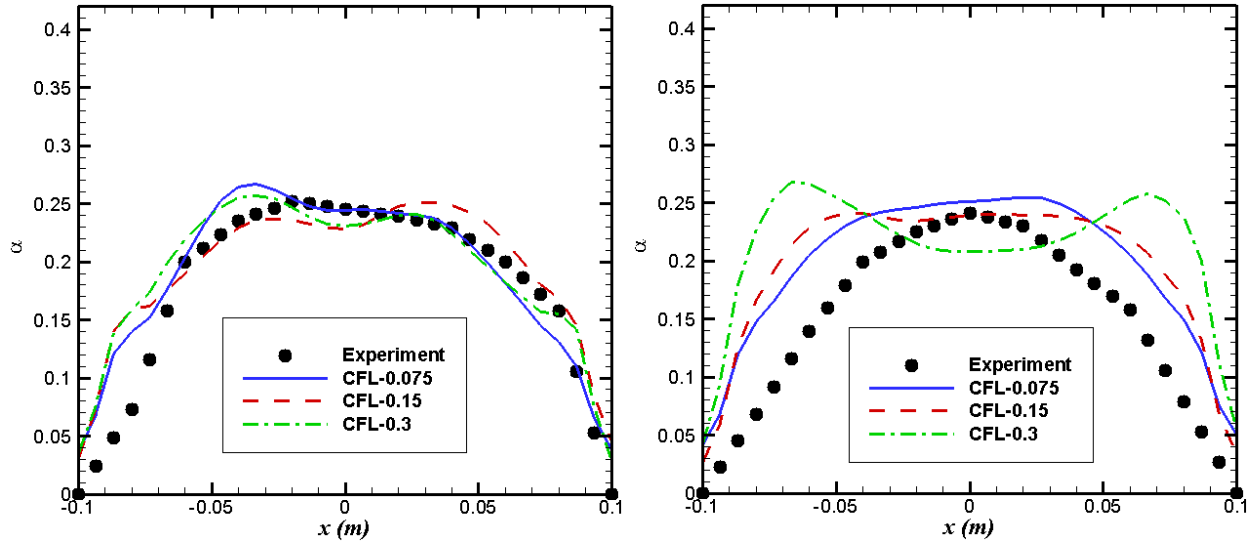
Figure 3.11: Air volume fraction profiles at (left) 0.15 m and (right) 0.65 m for cases testing the effects of the CFL number.

3.3.3. Miscellaneous Issues

In addition to the temporal and spatial aspects of the numerical model employed, there are also several other details that are important to the computational execution of the system.

3.3.3.1. Precision

Determining the precision of a calculation requires understanding the value of calculation time compared to accuracy. For most cases, single precision calculations, involving fewer equations, are sufficiently accurate and thus preferable. In the simulations conducted here, because of the two phases interacting and relatively narrow chamber diameter, the accuracy of double precision becomes crucial; therefore, the decision was made to use double precision and sacrifice calculation time for accuracy in all simulations.

3.3.3.2. Convergence Criteria

The convergence criteria determine what exactly should be considered converging data. In general, a drop in all residuals of at least three orders of magnitude per time step is considered

41

satisfactory convergence. In the calculations performed in this study, the decision was made to increase this value to four orders of magnitude to allow for enhanced convergence each time step. This ensures that truly converging data is provided and allows for additional time for the equations to settle. This inherently adds to the calculation time, but it is considered worth the sacrifice to improve the resulting data.

3.2.3.3 Iterations per Time Step

In conjunction with the convergence criteria, another factor is the designated maximum number of iterations allowed. This works with the convergence criteria to determine when it is appropriate to move on to the next time step. The next time step is reached when either the convergence criteria are fulfilled by all residuals dropping four orders of magnitude or when the maximum iterations per time step is reached. The default setting for this value is 20, but this is considered insufficient for the simulations being performed. The residuals would very rarely drop four orders of magnitude in this span, thus the equations were never truly converging, so it was decided to extend this value from 20 to 50. Increasing the number of iterations allows for the residuals to drop appropriately, thus improving the results. While 50 is a relatively high value, it did keep the calculation going at a reasonable pace if there were sections that had trouble converging, even after 50 iterations. This is particularly common at the beginning of most simulations, and so making this value any higher would slow the calculation down unnecessarily. Convergence criteria and the allowed iterations per time step are clear examples of the constant balance between calculation time and accuracy.

To summarize the conclusion of this large 2D parametric study, it was determined through both simulation validation and literature review, there are many important parameters

that are crucial to an accurate model. The effects of virtual mass, drift, and surface tension can be neglected. The Schiller-Naumann drag model is most appropriate. The dispersed $k - \varepsilon$ turbulence model should be employed. The most accurate discretization schemes are the Green-Gauss node based spatial discretization method and the modified HRIC volume fraction discretization method. A CFL of 0.075, relating to a time-step size of 0.005 s is determined to be appropriate. A grid resolution study revealed that the system is very sensitive to changes in grid density, and that the most appropriate resolution is 27x270. This was discovered in conjunction with a bubble diameter study that revealed a strong relationship between cell size, bubble diameter, and the resulting physical flow conditions.

3.4.   3D Bubble Column Case

This section will detail the development of the 3D bubble column model from the 2D model. Meshing, results, and post-processing will be summarized and presented.

3.4.1. Geometry and Meshing

To facilitate the transition from 2D to 3D simulations, the geometry is created to be as similar as possible to the 2D calculations for the bubble column. Therefore, the height and diameter of the 3D chamber match the dimensions of the 2D chamber. Inherently, due to the increased complexity of 3D models, the calculations take longer to run and the post processing is equally difficult.

The 2D grid resolution study is used as a guide, but the meshing techniques in a 3D cylindrical channel do not allow for a perfect replication of a 2D mesh. The meshing technique in the vertical direction (*z*), is the same as the vertical direction in the simple, 2D case (*y*). However, the base of the column (*x* and *y*) requires a non-uniform meshing technique. At first, a

43

standard "spoke-wheel" method of meshing the circular cross section is attempted, as shown in Figure 3.12.
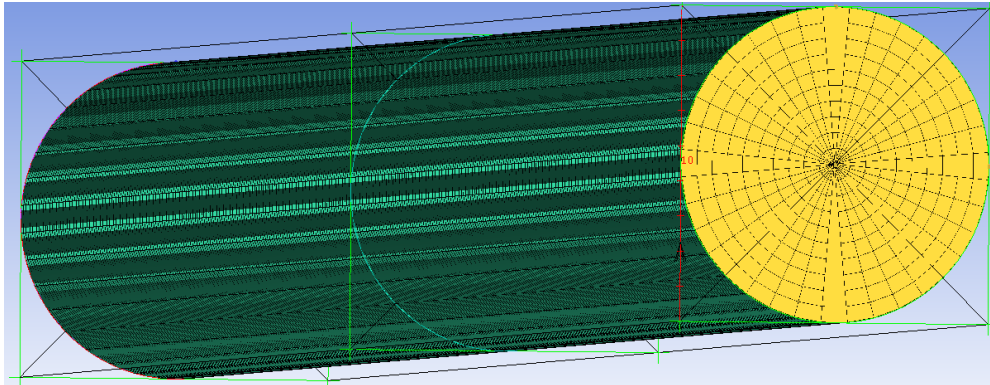
Figure 3.12: 3D geometry in ICEM displaying the "spoke-wheel" meshing style

Clearly, the mesh converges to a singularity at the center, and there is a large variance in grid size from the outer edge to the center of the channel. The singularity is problematic and prompted the exploration of alternative methods. The "O-grid" meshing scheme allows for removal the singularity at the center of the channel. While there is still variation in grid size, the average discrepancy is much lower, and the mesh can be seen in Figure 3.13. This scheme provides good results, and thus has been adopted as the standard meshing technique for all 3D bubble column cases for the remaining simulations.
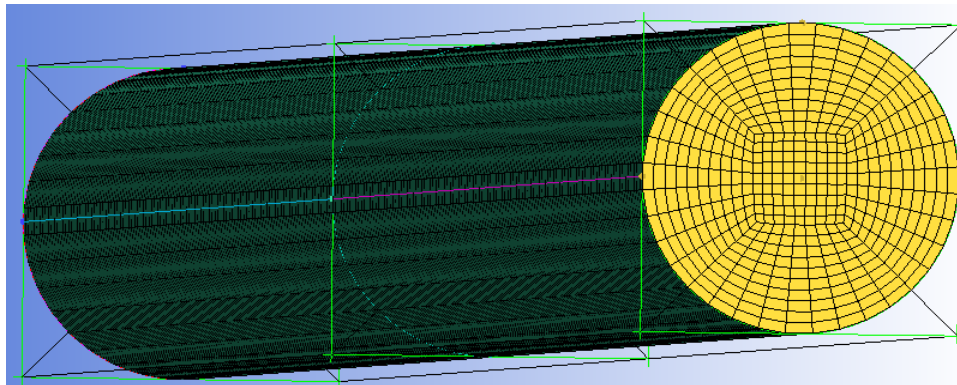
Figure 3.13: 3D geometry in ICEM displaying the "O-grid" meshing style

3.4.2. Spatial Averaging Results

An advantage of running simulations in 3D is that the entire physical domain can be captured, thus the laws of physics can be more appropriately applied. One challenge is increased computation time, but another is the challenge of visualizing data. It is straightforward to interpret 2D data, and so it is desirable to transform the 3D results into a 2D depiction. One solution is to select a vertical cross-section from the 3D geometry that has the same dimension as the 2D geometry (Figure 3.1). While this provides the benefits modeling the entire 3D regime, using the data from one cross-section neglects the vast majority of the computational space. The common solution to this issue is to incorporate spatial averaging to capture the full domain and utilize more of the flow field.

The technique of spatial averaging is utilized in the 3D bubble column solutions to more fully understand the results that are calculated, and to compare them to the 2D results. The number of planes required to be spatially averaged in order to properly capture the 3D effects is explored. While there is no limit to how many planes can be averaged, it does not make sense to average an exorbitant amount. The results of spatially averaging two, four, and eight planes are compared to the results of a single plane to see the effects and determine the appropriate number of planes to use. These planes are sampled evenly throughout the column by rotating around the centerline. To aid in visualizing the planes, a figure of the planes in the column can be seen in Figure 3.14.
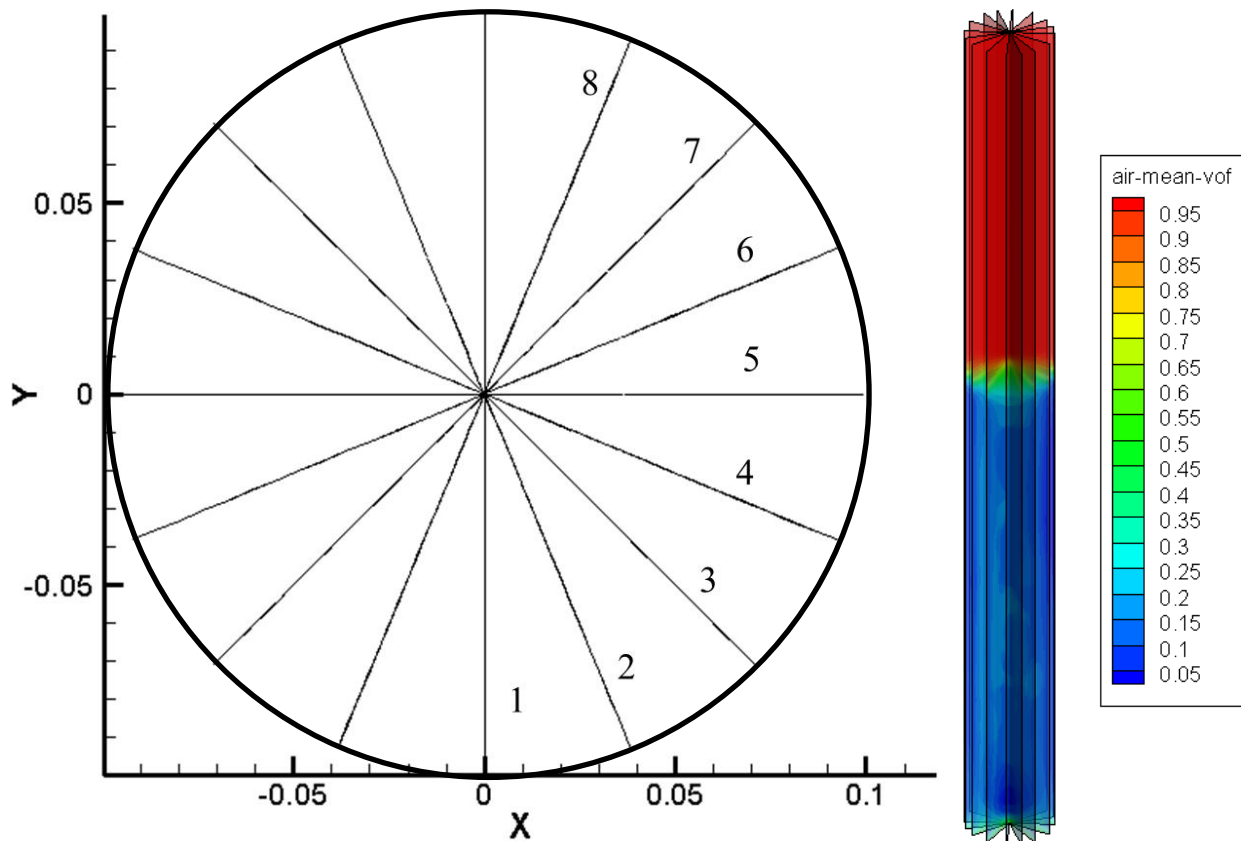
Figure 3.14: Planes used in the spatial averaging of the 3D bubble column results.

The x=0 is considered the 0° plane and is used as the plane of reference. The average of two planes includes plane 1 and 5 and the average of four planes includes planes 1,3,5, and 7. The results of the different spatial averaging can be seen in Figure 3.15, for the two column heights at which data has been collected. They support the claim that while some spatial averaging provides better representation of the 3D data, using more than two planes for this particular application does not yield a significant increase in precision. Therefore, for any additional 3D bubble column analysis, only two planes will be used in spatial averaging. This rule may not apply for less symmetric flows, flows with different time-averaging, or flows with largely different characteristics.
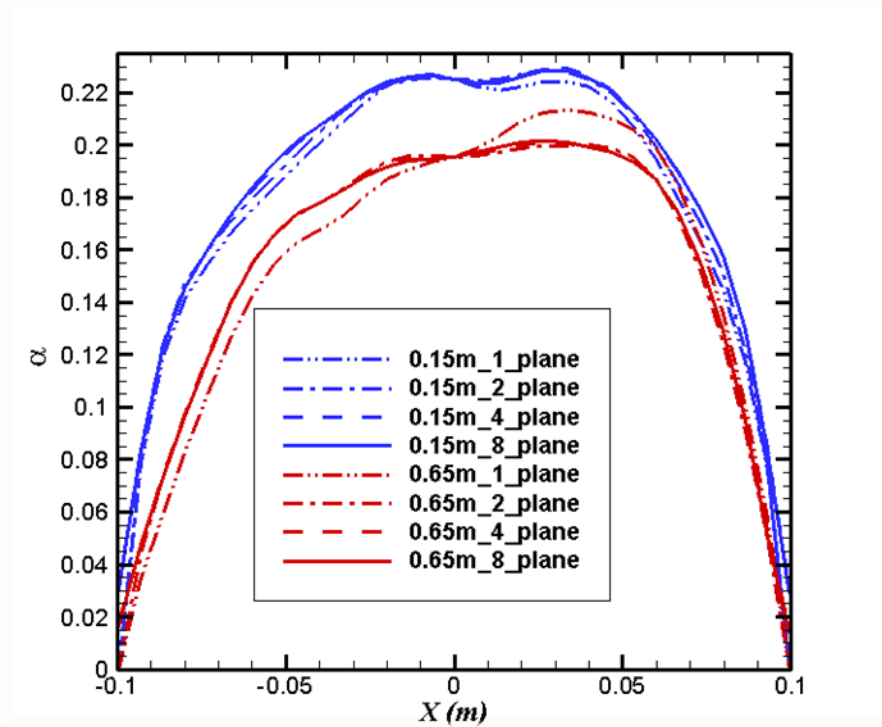
Figure 3.15: Comparison of different spatial averaging at both 0.15 m (blue) and 0.65 m (red) heights for the 3D bubble column.

3.4.3. Grid Convergence Index Study

With the spatial averaged results, a GCI study is performed to compare the results of different grid resolutions in the 3D simulations. Since the spatial averaging translated 3D data to 2D data, the GCI procedure followed in Section 3.3.1.2 applies here as well [10]. Since the grids are non-uniform, in order to keep a consistent r value, the number of nodes on the diagonal of the base are compared, as well as the nodes in the vertical direction. The grid resolutions compared are 20x200, 30x300, and 45x450, the same resolutions compared in the 2D study, representing the nodes along the diagonal by the nodes along the vertical. The comparison of the three resolutions tested can be seen in Figure 3.16 and a summary of the grid resolutions can be found in Table 3.3. These results show the effects of grid resolution, which are more quantitatively

47

explained in Table 3.4. It can be determined from Figure 3.16 that finer grid resolutions do not result in worse predictions in 3D cases.

Table 3.3: Explanation of 3D grid resolutions and comparison to 2D equivalents.

Resolution	Number of Cells	2D Equivalent
Coarse	46,800	20x200
Medium	162,000	30x300
Fine	310,626	45x450
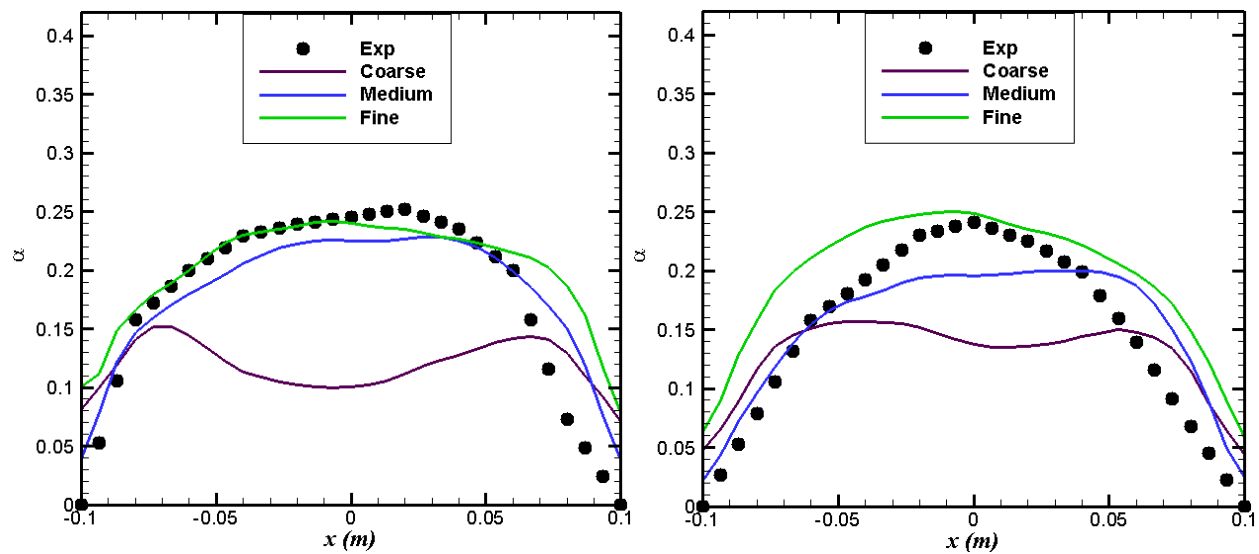
Figure 3.16: Air volume fraction profiles at (left) 0.15 m and (right) 0.65 m for cases testing effects of 3D grid resolution.

Table 3.4: 3D GCI results for air volume fraction

y	Coarse/Medium	Medium/Fine
0.15 m	0.60%	0.43%
0.65 m	1.89%	1.47%

These GCI results are more straightforward to interpret. At both channel heights tested it can be seen that the percent error between cases decreases as the grid becomes finer. It seems that the issues with an overly fine mesh are limited to 2D cases, and when brought into a 3D geometry the physics of the problem are more well behaved. These results are consistent with

the profiles observed in Figure 3.16. While finer cases, such as a 60x600 equivalent, would be interesting to compare to see if there is a limit to the improvement of fine resolutions, this case would be extremely computationally expensive. For comparison, a 2D 30x300 case takes about 16 wall clock hours to simulate 90 seconds on a single processor. The 45x450 equivalent 3D case takes 94 days to simulate 90 seconds using one processor on the same machine. This is a difference of 140 times, and is a large reason why 2D simulations of bubble columns are so commonly used. Figure 3.17 compares the results of the 2D and 3D cases, and the results show that there are not significant improvements warranting the additional computational time.
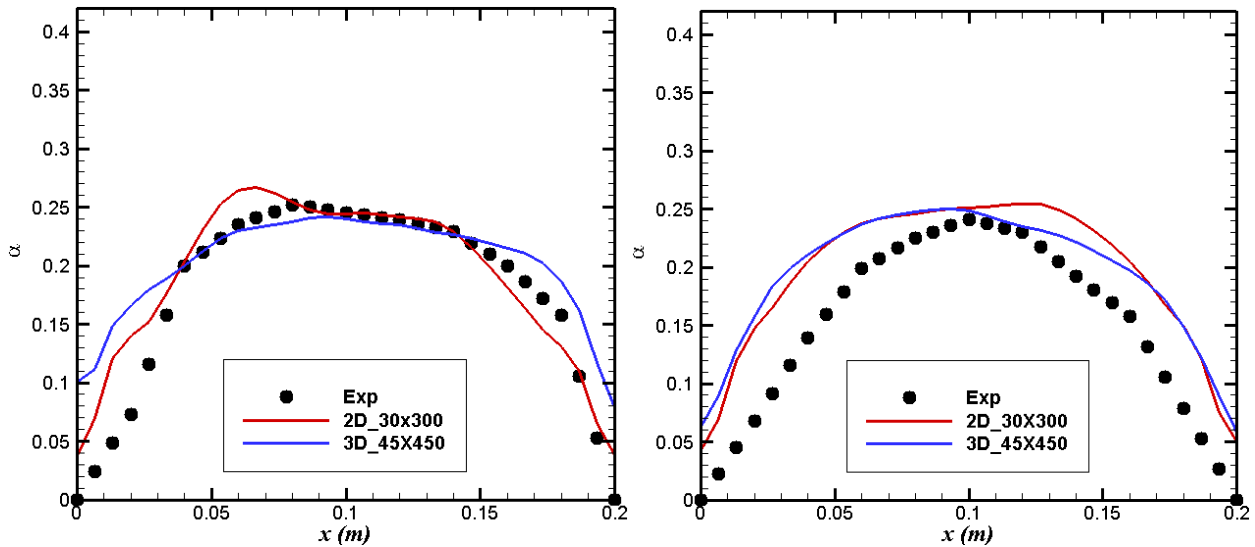
Figure 3.17: Air volume fraction profiles at (left) 0.15 m and (right) 0.65 m for 2D and 3D cases.

Chapter 4. Microbial Fuel Cell

This chapter introduces the MFC geometry and presents the results of the first simulations run using chemical reactions and the spiral spacer. A parametric study is summarized and both 2D and 3D results are displayed.

4.1.   Background

The MFC reaction chamber is a three-dimensional cylinder that houses a spiral spacer (section of bristles) and is primarily filled with water. A schematic and photograph of the MFC is shown in Figure 4.1. The photograph shows the MFC designed and tested by Dr. He's research team in Civil Engineering. The purpose of this fuel cell is to intake untreated water and treat is by passing it through a colony of micro-organisms that feed on the undesired particles, in this case acetate, in the water. This is achieved by a chemical reaction, in which the acetate (CH_3COO) is oxidized and the water leaves the system treated to an acceptable level [16]. The chemical equation is detailed in future sections of this document, but it is important to understand that this drives the effectiveness of the MFC. At times, based on the concentration of acetate in the water sample and the size of the microbial colony, a second pass through the reaction chamber may be required.

The second desirable outcome of this chemical reaction is that free electrons are emitted. The micro-organisms live on bristles attached to a copper wire, which acts as the backbone to the entire spiral structure within the chamber. When the free electrons are emitted from the reaction, the copper wire, being very conductive, captures them and channels them into a circuit, producing usable electricity. The entire function acts like a battery, with an anode, cathode, and electrolyte. Electrons released in the reaction are transferred through the anode to the cathode, where they are either operated in a working current or are transferred to a material containing a

resistor [16, 26]. Currently the energy gains from this process are modest, but with an investigation on how flow characteristics can enhance or detract from the reaction rate within the chamber, it may be possible to improve these gains significantly.

While the entire design is very detailed, this investigation is only concerned with the reaction chamber. The geometry of this chamber strongly resembles the geometry used in the 3D bubble column. The reaction chamber at its simplest form is a cylindrical tube that houses a flexible spiral spacer, shown in Figure 4.2. The spacer acts to direct the flow in a helical pattern from the bottom of the chamber where it is introduced, to the top where it exits. The chamber is 50 cm tall and only 4.2 cm in diameter, making it shorter and much narrower in size compared to the bubble column in Chapter 3. In addition to the chamber and spacer, there are also bristles attached to a copper wire that stretch along the centerline of the channel.
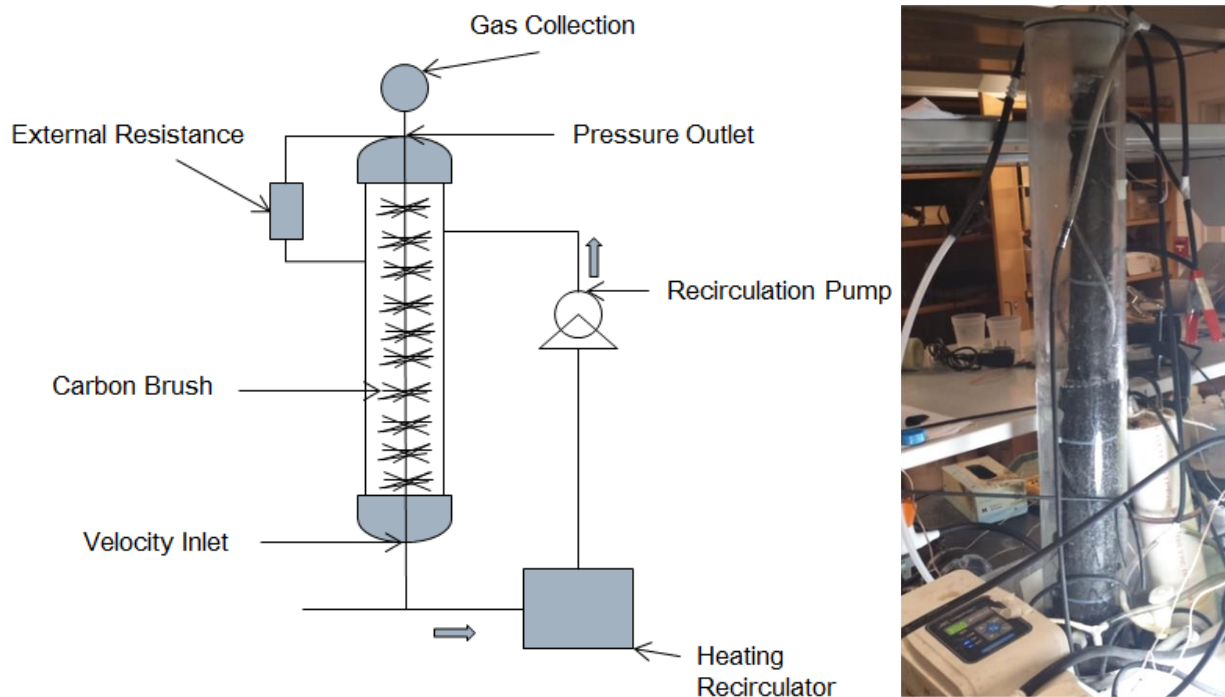
Figure 4.1: Schematic of the MFC reaction chamber [18] (left) compared to actual photograph of the tabletop apparatus (right).

This part of the structure is neglected for this study, but it is proposed that in future research the bristles be included in the model. Now that the system has been introduced, it is important to understand how the geometry is created and meshed before simulations could occur.

Figure 4.2: Photograph of the spiral spacer removed from the reaction chamber.

4.2. Modeling the MFC System

Modeling the spiral in ANSYS ICEM software is not a trivial task. Until this point, all the modeling presented (Chapter 3) is fairly simple and does not pose any issues. The complexity of the spiral spacer demanded a higher level of modeling, especially creating the mesh.

4.2.1. ICEM meshing methods

The geometry of the chamber walls is simply the geometry of the 3D bubble column, but with different dimensions. The spacer, though in reality not evenly distributed, is considered to be a 2D spiraling plane with no thickness stretching from the inlet to the outlet of the chamber. It is created by calculating points along the outside wall of the chamber and creating a spiraling line along the circumference. These points are connected and formed into a plane that channels the flow up through the chamber. Visually this resembles the spacer in Figure 4.2. The size and shape of the spacer created in ICEM can be seen in Figure 4.3. The outer rim of the spiral has a length of 2.14 m, and the length of the centerline of the spiral is 1.22 m, for a total of 16 spirals.
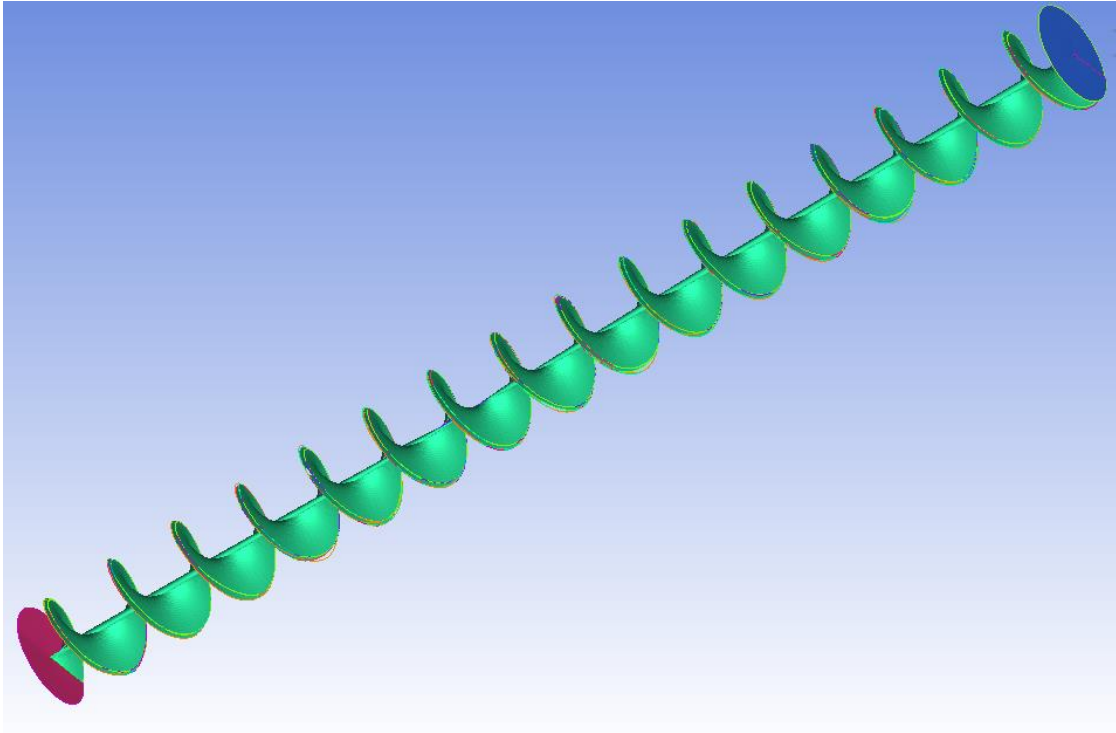
Figure 4.3: Full spiral geometry of the MFC that is used in the Fluent simulations.

The issue is that since the spacer is infinitely thin, the meshing did not treat it as a wall and the flow passes through the chamber as if the spacer is not there. It was determined that it would be necessary to model the spacer with a finite thickness. After convening with the VT Civil Engineering team and measuring the thickness of the spacer they are using, a value of 1.8 mm is used and the new spacer is created. Unfortunately, ICEM was not able to properly mesh this new and increasingly complex object. Even when meshing the spacer and chamber separately and then overlapping them, the simulations would not run.

4.2.2. Fluent Meshing Methods

The solution to the meshing problem came by turning to Fluent's meshing program in the latest version (15.0). This allowed for a more general meshing technique to be applied, rather

than selecting the number of nodes used by each edge. While this did not allow for the level of control that ICEM meshing provides, it does enable the new object to be meshed.

Unfortunately, even with the improved meshing scheme, the flow was ignoring the spacer presence and traveling upward through the channel as if it were an empty cylinder. The final solution came later when it was realized that instead of adding the spacer to the geometry, the spacer could be removed from the geometry and the gap could be void space that is not included in the computational domain. The approach worked and the flow is forced to travel in the helical pattern, just as it would with the spacer present. Figure 4.4 shows the absence of the; with the revised geometry, the model is ready to be used to simulate MFC cases.
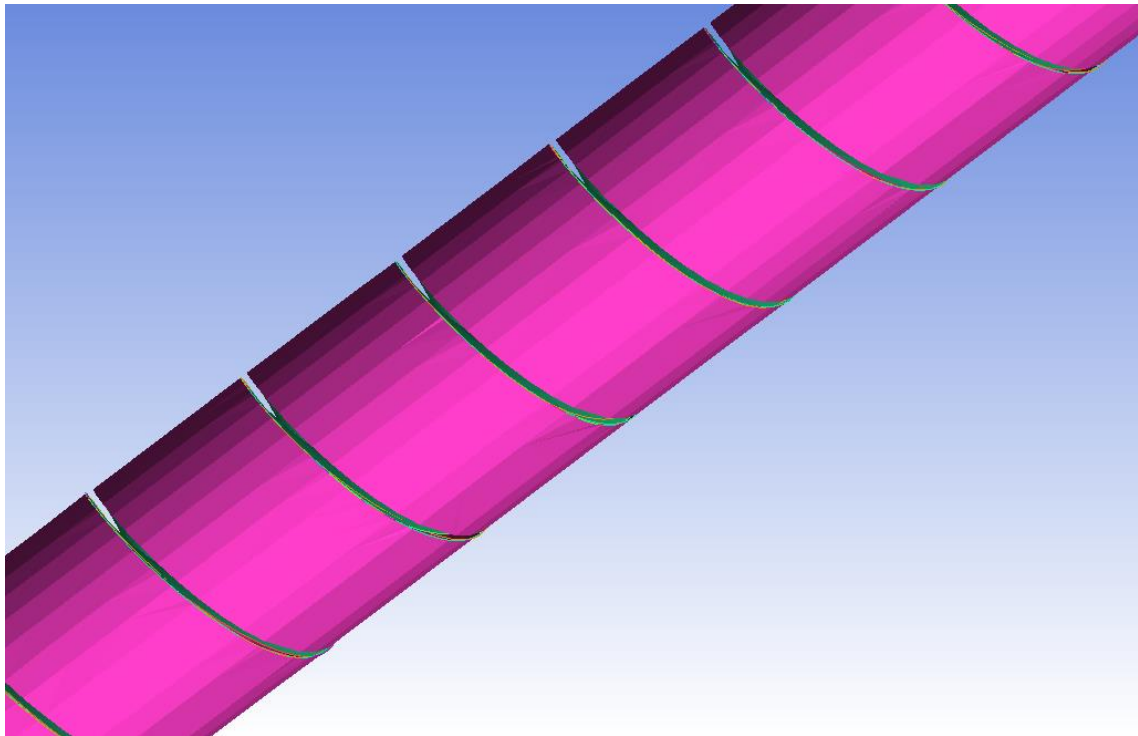
Figure 4.4: Fluent based geometry with spiral spacer removed from the column

4.2.3. Non-Reacting Simulations

The first cases run using the revised 3D geometry do not include chemical reactions. To ensure that the geometry is correct, a simple single-phase, non-reacting flow is simulated in order to observe that previous issues had been overcome and that the flow is behaving in a physical manner. The streamlines of the first successful simulation in the 3D MFC geometry are shown in Figure 4.5. These results confirm that the flow is recognizing the presence of the spacer, and traveling the appropriate path to the top of the chamber. With these results confirmed, the more complex simulations are ready to be tested.

Figure 4.5: Streamlines of velocity magnitude for the non-reacting 3D MFC simulation.

In the sections to follow, there are several geometries that are used in simulations, and it is important to understand the differences when making comparisons between geometries. The 2D and 3D empty column cases all use the same geometry as the bubble column cases: 2 m height and 0.2 m diameter. These geometries are meshed with a 2D 30x300 grid and a 3D 30x300 equivalent grid density (Table 3.3). It is appropriate to compare to the shorter (0.5 m) 3D MFC geometry since the spacer increases the distance the average particle must travel to exit the channel. Because the distance along the outside of the spacer is 2.14 m and the distance close to the spacer center is 1.22 m, the comparison to the 2 m high channels represents a similar distance. While these numbers do not perfectly match the taller geometries, they are considered close enough to learn from the trends observed in these simulations. There are also issues that occur when comparing 2D and 3D geometries because the 2D cases do not have a volume. The 3D geometries have an actual volume calculated by the base times the height. In order to simulate comparable 2D and 3D results, the 2D results must be multiplied by πR^2, and for the 2D geometry, $R = 0.1$ m. Also, since the diameters for the two 3D geometries have different are different (0.2 m and 0.042 m) adjusted legend ranges for acetate concentration must be used for a direct comparison. For simplicity, a factor of 20 will be applied to the range all 3D empty column cases, and a factor of 4.2 will be applied to the range of all 3D MFC acetate concentration contours. To get a simple value to adjust the ranges by, when comparing a 2D case to a 3D empty column case, the range of acetate concentration must be multiplied by 0.00157 and when comparing a 2D case to a 3D MFC case, the acetate concentration range must be multiplied by 0.00748. This will account for the different dimensions and allow for a more appropriate comparison. This comparison will only affect the concentration contours displayed later in the chapter since these have a volume term in the units.

4.3.   Chemical Reaction

The chemical reaction that occurs within the reaction chamber is responsible for creating

the MFC as an effective and interesting piece of equipment. The reactions allow for the

beneficial effects of removing the acetate from the untreated water as well as the production of

free electrons. The process is based on the oxidization of acetate, which can be modeled as [16]:

$$CH_3COO^- + 4\ H_2O \leftrightarrow 2\ HCO_3^- + 9\ H^+ + 8\ e^- \qquad (4.1)$$
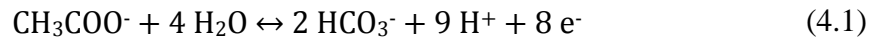
Equation 4.1 is a balanced reaction that seems to be stable, but these ionic elements and

compounds are not stable in mixtures. They require an oppositely charged particle with which to

bond in order for the mixture to be stable in the natural world. With the advice of the Civil

Engineering team, the bulk bonding element selected is sodium, as this provides a very favorable

chemical balance, and sodium acetate is commonly found in untreated mixtures. Introducing

sodium to the reaction provides a similar, but adjusted equation:

$$Na + NaCH_3COO + 4\ H_2O \leftrightarrow 2NaHCO_3 + 9\ H^+ + 8\ e^- \qquad (4.2)$$

Equation 4.2 will be modeled in Fluent to simulate and predict the fluid flow through the MFC.

While the background work for this problem was performed using two-phase flow

models, it was determined after learning more about the MFC that the interesting part of the

process is the chemical reactions, and not the interaction of phases, but rather species. This

being stated, it by no means negates the relevance of the work performed in the multiphase

domain, which helped validate models and deepen the understanding of flows through

cylindrical chambers. It also provided a means to become adept with the necessary software

programs and instilled an appreciation for how to recognize flows as either physical or non-

physical. The remainder of this chapter will discuss the processes, challenges, and results of modeling this chemical reaction.

4.3.1. Defining the Compounds

The Fluent materials database contains many compounds and their properties that are frequently used for chemical reactions. The compounds required for Equation 4.2 are not in the Fluent database, and requires user definitions, which is a rather tedious process of creating a new material and associated chemical properties. The specific properties are for sodium, sodium acetate, and sodium bicarbonate, and three user-defined materials are created [27-29]. The properties gathered from these resources are listed in Appendix A. With the ability to now use these compounds, the appropriate reaction can be modeled.

4.3.2. Modeling the Reaction

As has been the methodology throughout this study, whenever introducing a complexity to the system, it is best to begin with the most simple cases. All cases are initialized with a channel completely full of water and a mixture of water, sodium, and acetate is introduced at the inlet. Preliminary work begins using a 2D model of the MFC system for chemical reactions. Reacting flow is simulated using the rectangular column geometry used in the 2D bubble column cases (Figure 3.1). These cases run much quicker than those in the larger, more complex, 3D geometries; therefore, troubleshooting is easier and allows for faster feedback. After creating the necessary compounds for the reaction equation, careful attention is paid to appropriately simulate chemical reactions [20].

The Arrhenius expression used to model the reaction is:

$$k_r = A_f T^b e^{-\frac{E_r}{RT}} \hspace{4cm} (4.3)$$

where k_r is the reaction rate constant, A_f is the pre-exponential factor, b is the temperature exponent, E_r is the activation energy, R is the universal gas constant, and T is the temperature. Using Equation 4.3 and a study by Zielinksi, M. [30], the reaction is able to be initialized in Fluent.

The initial and boundary conditions for the simulation assumes a temperature of 300K and inlet velocity of 0.00002 m/s. The very low inlet velocity is derived from the industry standard provided by the VT Civil Engineering team for MFCs where the hydraulic retention time is 8 hours. Using the volume of the entire channel and the surface area of the inlet, an inlet velocity is calculated to be very close to 0.00002 m/s. The retention time is quite similar to those used in industrial applications, although there is much interest to see if it would not be beneficial to adjust the standard retention time [31]. Note that for larger geometries, the inlet velocity will increase, since the hydraulic retention time is constant, regardless of geometry size. With the inlet velocity of 0.00002 m/s and the diameter of the channel of 0.042 m, the Reynolds number is approximately 1, and laminar flow is modeled. The Civil Engineering team provided the concentration levels of sodium acetate entering the chamber at approximately 0.5g/L of solution. The three parameters that define the base case have been introduced. The three parameters that will be varied and investigated through the remainder of this chapter an inlet velocity of 0.00002 m/s, an initial acetate concentration of 0.5 g/L, and a temperature of 300 K.

4.3.3. Base Case Results

The results shown in Figure 4.6 are simulated for two cycles of the flow, equal to twice the hydraulic retention time, which will be applied to all cases. Therefore, even if the velocity increases, there is some commonality between all cases so comparisons are able to be made. Figure 4.6 presents the instantaneous results of the 2D base case after two retention periods (16 hours). The contours on the left show the molar concentration of acetate and the contours on the right display the reaction rate in the chamber. As expected, near the inlet, where the acetate is being introduced, the acetate concentration and reactions are highest. This is represented by the regions of red and orange contours. The results show that a reaction is indeed occurring, and that the system is ready to be simulated in 3D with the complexity of the spacer included. Throughout this study, the two values of molar concentration of acetate and reaction rate will be investigated, as these are the most important units to track. Interpreting the contours of acetate concentration will determine if acetate is exiting the reaction chamber, and studying the reaction rate contours will aid in understanding in what region and at what rate the reactions are occurring. In the following section, the results of the numerous cases simulated will be presented and analyzed.
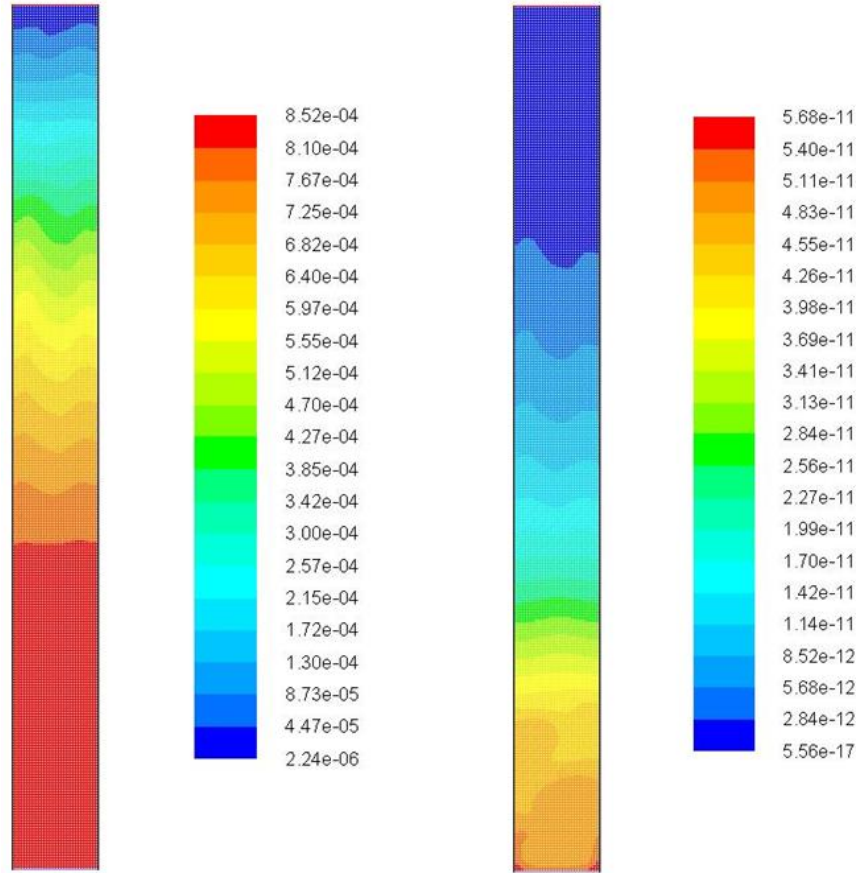
Figure 4.6: Contours of molar concentration of acetate (left) in kmol/m^3 and reaction rate (right) in kg·mol/(m^3·s) for the 2D base case.

Incorporating all of the parameters and initial conditions into the 3D system is not as difficult as anticipated due to the significant troubleshooting that was performed in the 2D cases and the development of the complex 3D geometry. Using all of the specified base case initial conditions, the first 3D reacting case is simulated. The streamlines presented in Figure 4.7 display that the flow in the reacting channel is behaving in a very similar manner to the flow in the non-reacting case (Figure 4.5), as is expected. The results in Figure 4.8 show that for the base case, all of the reactions and all of the acetate remain in the lower portion of the reaction chamber. While this case is not particularly interesting, it will be intriguing to see how varying some of the parameters affects the flow.

61

Figure 4.7: Streamlines of velocity magnitude for the reacting MFC system.

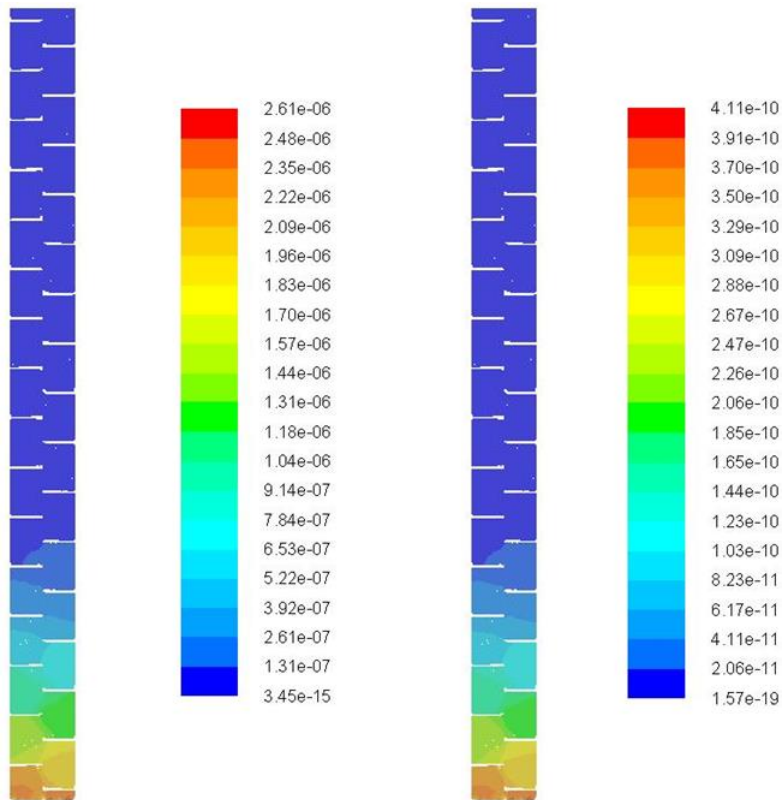| 2.61e-06 | | 4.11e-10 |
2.48e-06		3.91e-10
2.35e-06		3.70e-10
2.22e-06		3.50e-10
2.09e-06		3.29e-10
1.96e-06		3.09e-10
1.83e-06		2.88e-10
1.70e-06		2.67e-10
1.57e-06		2.47e-10
1.44e-06		2.26e-10
1.31e-06		2.06e-10
1.18e-06		1.85e-10
1.04e-06		1.65e-10
9.14e-07		1.44e-10
7.84e-07		1.23e-10
6.53e-07		1.03e-10
5.22e-07		8.23e-11
3.92e-07		6.17e-11
2.61e-07		4.11e-11
1.31e-07		2.06e-11
3.45e-15		1.57e-19

Figure 4.8: Contours of molar concentration of acetate (left) in kmol/m^3 and reaction rate (right) in kg·mol/(m^3·s) displayed on the x and y axis for the MFC.

When making comparisons between the reaction rates for 2D and 3D predictions (Figures 4.6 and 4.8 respectively), the reaction rates seem quite similar. That is because the units of reaction rate include a time term, and since all cases are comparable in the sense that they are all run to twice the hydraulic retention time, these results can be compared. For the acetate concentration results, the magnitudes are several orders of magnitude different. This is because the units do not include a time term, only volume. When calculating the volume of a 2D surface, the units are per unit depth. As was mentioned in the previous section, an adjusted range must be used to compare the acetate concentration results between 2D and 3D cases. In the following sections these comparisons will be made, and the adjusted range will be employed.

4.4. Parametric Study

Several parameters are investigated in further detail to see how they affect the flow characteristics and the reactions occurring in the chamber. While there are many parameters that contribute to the flow, the three that were determined to be easy to adjust, have significant impact on the flow and reactions are the inlet velocity, the temperature, and the initial concentration of acetate in the system. The VT Civil Engineering team provided their input as to which factors may also contribute and be interesting to study. They agreed that inlet velocity and concentration would have interesting effects, and while they had doubts about the effect of temperature, it is deemed to be important for expanding understanding of the system, even if it would not be applied to the actual fuel cell system. A table of the cases included in the parametric study is presented in Table 4.1. The case numbers will be used as a reference throughout the parametric study. In addition, in order to emphasize the trends and comparisons from one parameter study to another, different legends are used for different figures. Because of

63

this, the base case will not always appear with the same contour level ranges for each comparison, even though the data has not been changed.

Table 4.1: Parametric study cases for inlet velocity, acetate concentration, and temperature comparisons.

Case	Inlet Velocity (m/s)	Acetate Concentration (g/L)	Temperature (K)
Base Case	0.00002	0.5	300
Case 1	0.0002	0.5	300
Case 2	0.002	0.5	300
Case 3	0.02	0.5	300
Case 4	0.00002	0.5	350
Case 5	0.00002	0.5	400
Case 6	0.00002	0.5	500
Case 7	0.00002	0.25	300
Case 8	0.00002	1	300
Case 9	0.00002	2	300

4.4.1. Inlet Velocity Study

The first study is to evaluate the inlet velocity, which is a function of the size of the reaction chamber, assuming that the industry standard hydraulic retention time of 8 hours is followed. Three cases (1-3) are simulated holding all other parameters equal, but increasing the inlet velocity by an order of magnitude for each subsequent case. All cases are 2D, as these simulations run more quickly and allow for more rapid evaluation. The results of this study are summarized in Figure 4.9 for acetate concentration and reaction rate. These results show that inlet velocity does have a strong and noticeable impact on the reaction occurring within the chamber. As the velocity increases, the reactions begin to occur farther up the channel and at a higher rate. What is interesting is that in the cases with lower inlet velocities (Figure 4.9 (a) and (b)), it seems that the acetate is more highly concentrated at the bottom of the channel while this is reversed for cases with a higher velocity (Figure 4.9 (c) and (d)). The higher inlet velocity pushes the acetate farther up the channel before it is able to completely react; however, based on

the contour levels it is apparent that while the concentration of acetate is higher farther up the channel, the total amount of acetate in the system seems to decrease as velocity increases, which is represented by the green and blue contours. This shows that the increased reaction rate is eliminating the acetate. Therefore, while there is some acetate leaving the system, the concentrations are lower when an inlet velocity as high as 0.02 m/s is used (Figure 4.9 (d)).

As inlet velocity increases, the residuals for each case converge more consistently, resulting in a more reliable model. These factors recommend using a higher inlet velocity to increase reaction rate as long as some amount of acetate is acceptable to leave the system. When 3D results are observed later in this chapter, the problem of acetate leaving the channel is not observed. Also, if using multiple pass-throughs, a higher inlet velocity for the first pass would allow for rapid elimination of most of the acetate, and then feeding into a slower inlet to eliminate the rest of the acetate could be an effective method. Multiple pass-throughs is a fairly common practice when using MFCs, but the most efficient operating conditions would be those that do not require a second or third pass.
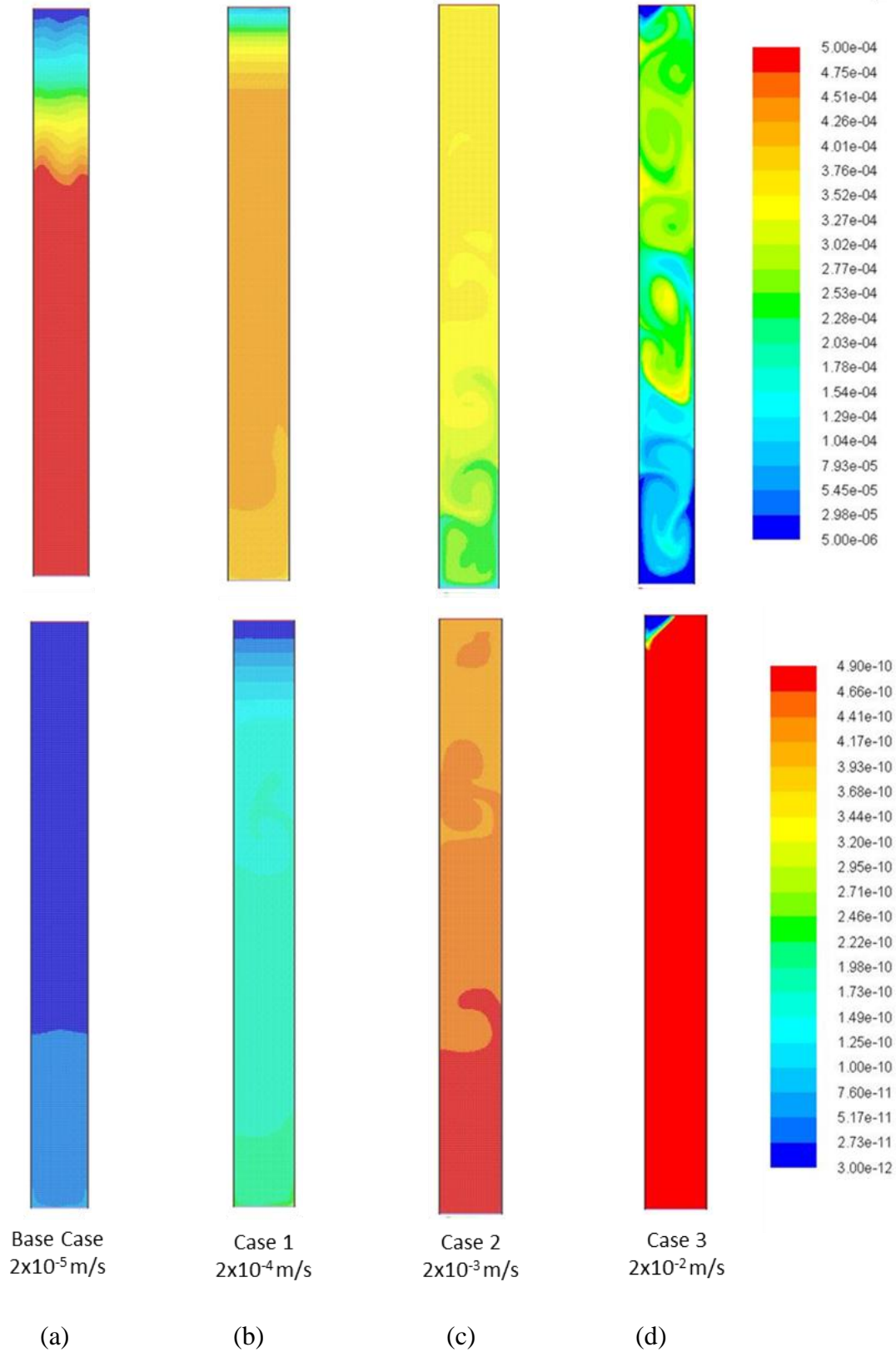
Figure 4.9: Contours of acetate molar concentration (top) in kmol/m^3 and reaction rate (bottom) in kg·mol/(m^3·s) to compare effects of velocity.

66

4.4.2. Temperature Study

Temperature is also isolated and tested as a parameter of interest in this study. The reactor used by the VT team of Civil Engineers functions at a temperature of roughly 300 K. While this is the temperature at which simulations are most useful, it was determined that it would be interesting to test cases run at higher temperature. Predictions at 350 K , 400K, and 500K (cases 4-6) can be seen in Figure 4.11 (b-d). The contours show that temperature does not make a tremendous difference in the reaction rate. Observing the acetate concentration reveals that as the temperature increases, the acetate in the system tends to decrease. A trend for maximum acetate concentration versus temperature is shown in Figure 4.10.
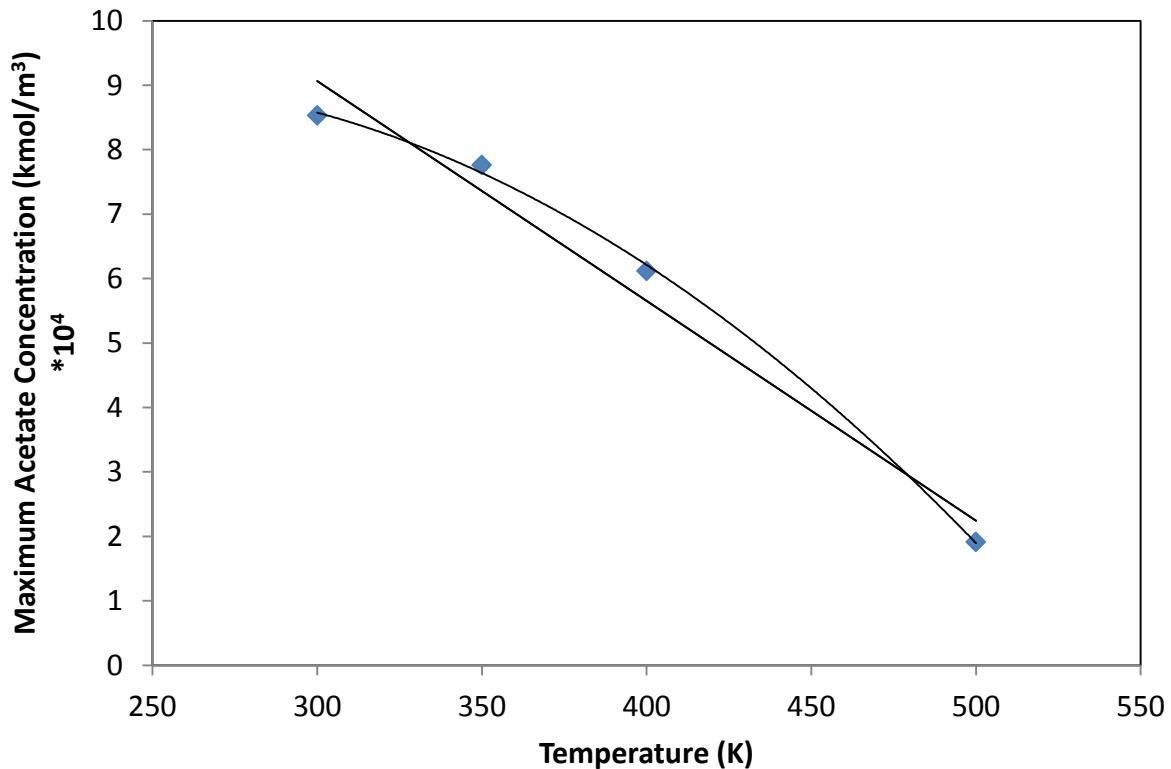

Figure 4.10: Relationship between system temperature and maximum acetate concentration for 2D analysis.
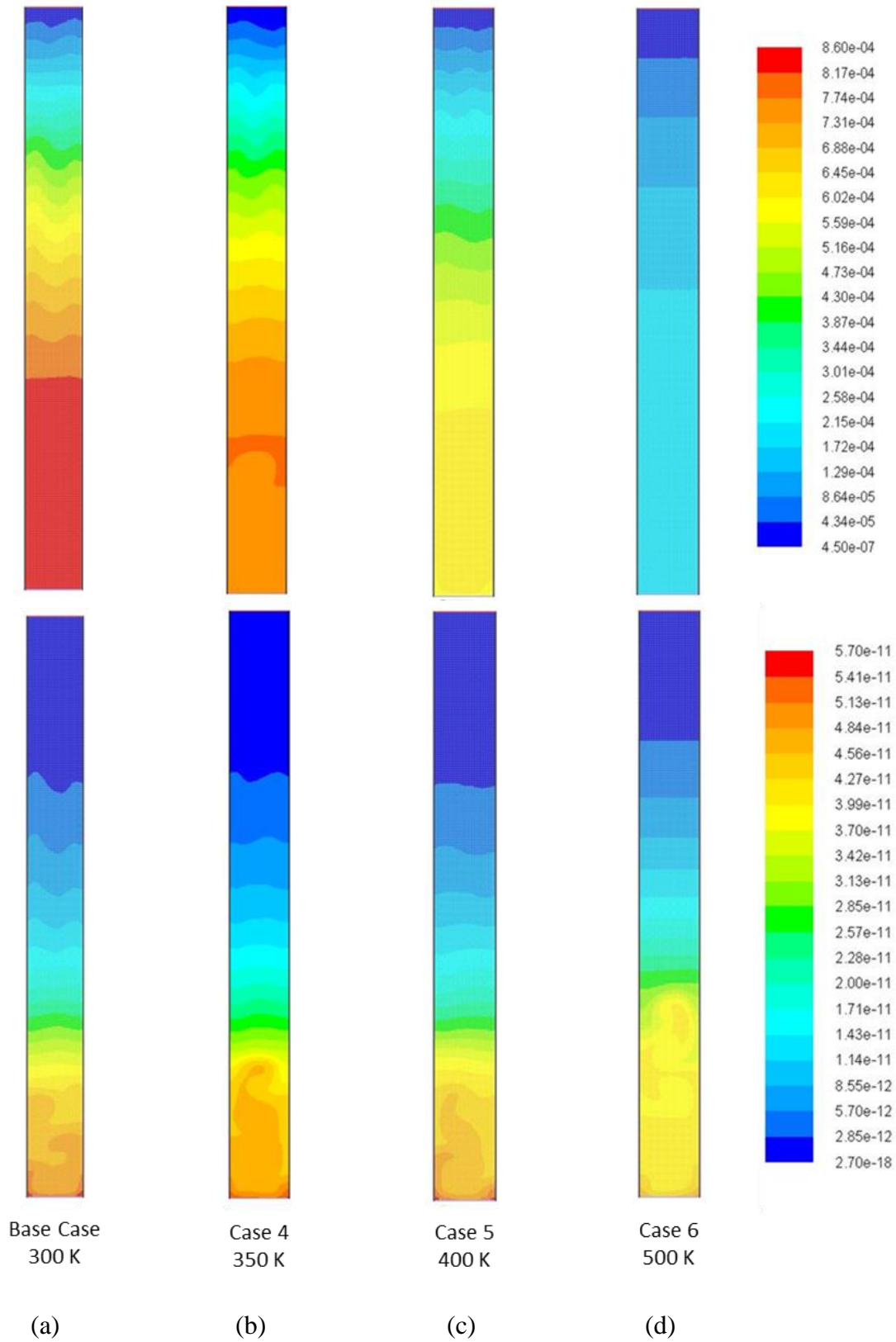
Figure 4.11: Contours of acetate molar concentration (top) in kmol/m^3 and reaction rate (bottom) in kg·mol/(m^3·s) to compare effects of temperature.

Base Case
300 K

Case 4
350 K

Case 5
400 K

Case 6
500 K

(a)

(b)

(c)

(d)

Both linear and polynomial trends are fit to the data and the linear trend is represented by $C_A = -0.0341T + 19.295$, with an R^2 value of 0.9704. Here, C_A is the concentration of acetate and T is the temperature. The polynomial trend, however, provides an even stronger explanation of the data. With an equation of $C_A = -0.0001T^2 + 0.0447T + 3.952$ and an R^2 value of 0.999, the line fits the data nearly to perfection. Clearly there is a relationship between temperature and acetate concentration such that as temperature increases, maximum acetate concentration decreases, but in order to confirm the nature of this relationship, more cases will need to be run.

In all cases, most of the acetate has reacted and been consumed from the system before it reaches the top of the channel. For the highest temperature (Figure 4.11 (d)), the acetate concentration near the inlet is lower than other cases, hinting that the reactions are occurring in greater quantities lower in the channel. When observing the contours of reaction rate, it can be seen that the region of higher reaction rates is larger, although slightly smaller in magnitude, in the 500 K (Figure 4.11 (d)) case compared to the others. This corresponds to the lower acetate concentrations since much of it is being consumed by the reactions occurring in this larger region of high reaction density. There is very little difference between these cases otherwise, and confirms that the VT Civil Engineering team is correct in their assumption that temperature would not greatly affect reaction rates.

4.4.3. Concentration Study

The final parameter studied is the initial concentration of acetate introduced to the system. The solution is primarily water, with traces of sodium and acetate specified based on recommendations from the VT Civil Engineering team. Clearly reaction rates will change based on varying concentrations of acetate, so cases are considered that simulate both lower and higher levels of acetate in the solution entering the system. The base level provides 0.5 g/L, but cases

of 0.25 g/L, 1 g/L and 2 g/L (Cases 7-9) are also tested. The results of this investigation are presented in Figure 4.12 (a, c-d).

Observing the contours of acetate concentration, all cases seem to have very similar patterns. Regardless of the concentration, it seems that virtually all of the acetate was eliminated before it reached the top of the channel. The contours of reaction rate show a more interesting trend. By observing the reaction rates as concentration increases, it can be seen that rates increase as well as the region in which reactions are occurring. For all cases, reactions occur at the greatest rate at the inlet of the chamber, as to be expected. While this information cannot be observed without looking more closely at the data, the maximum reaction rate for each case varies linearly with the initial concentration, as shown in Figure 4.13. A line fit to the data is of form $k_{max} = 1.1003C_A + 0.013$, expressing that for each unit the acetate concentration increases, the maximum reaction rate increases by a factor of 1.1. Also, an R^2 value of 0.9999 gives strength to support this claim for linearity. While testing more cases to see if this trend holds for different concentrations of acetate would be interesting, the fact that there is evidence of a linear relationship with the data is undeniable.
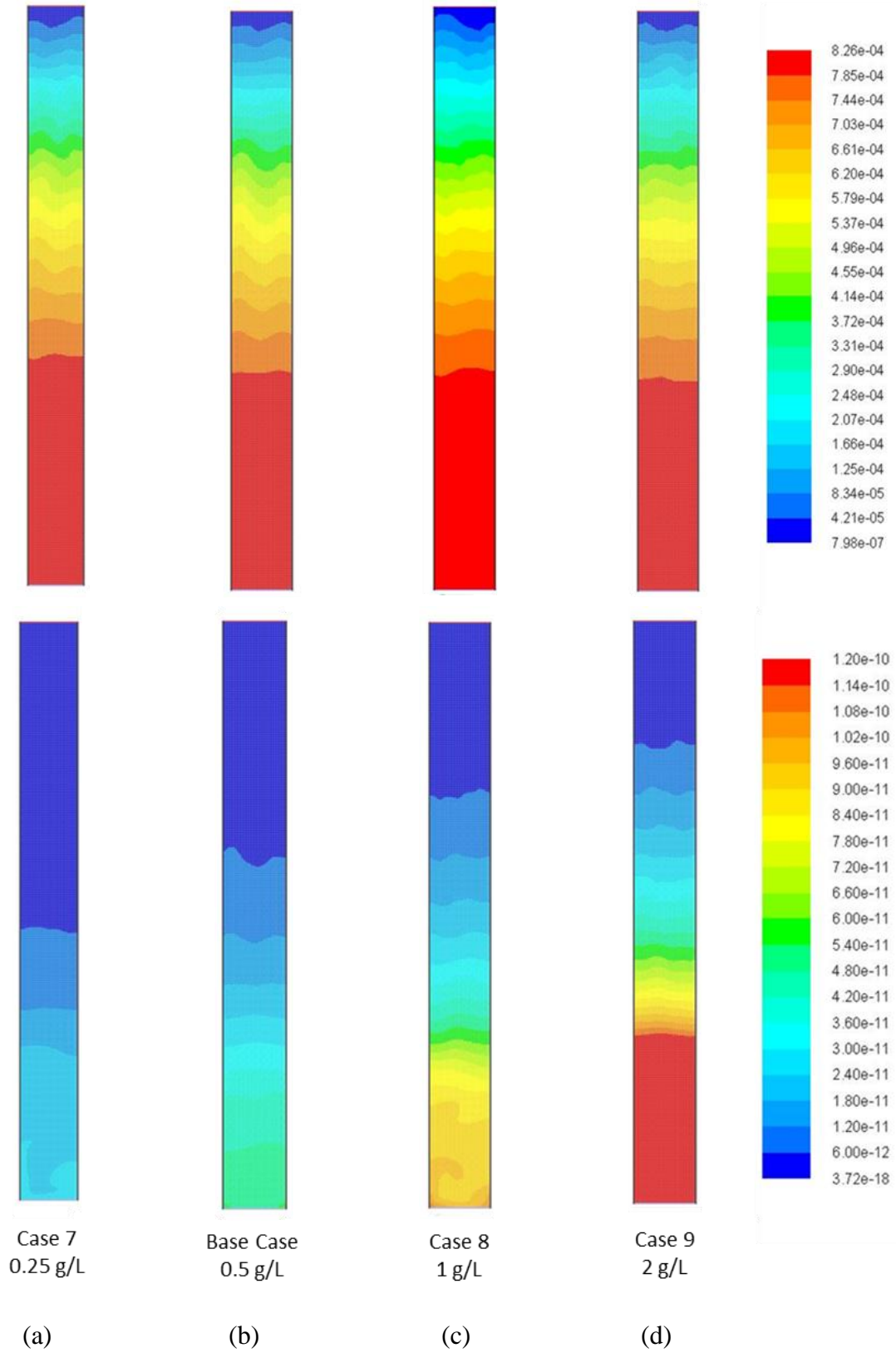
Figure 4.12: Contours of acetate molar concentration (top) in kmol/m^3 and reaction rate (bottom) in kg·mol/(m^3·s) to compare effects of concentration.
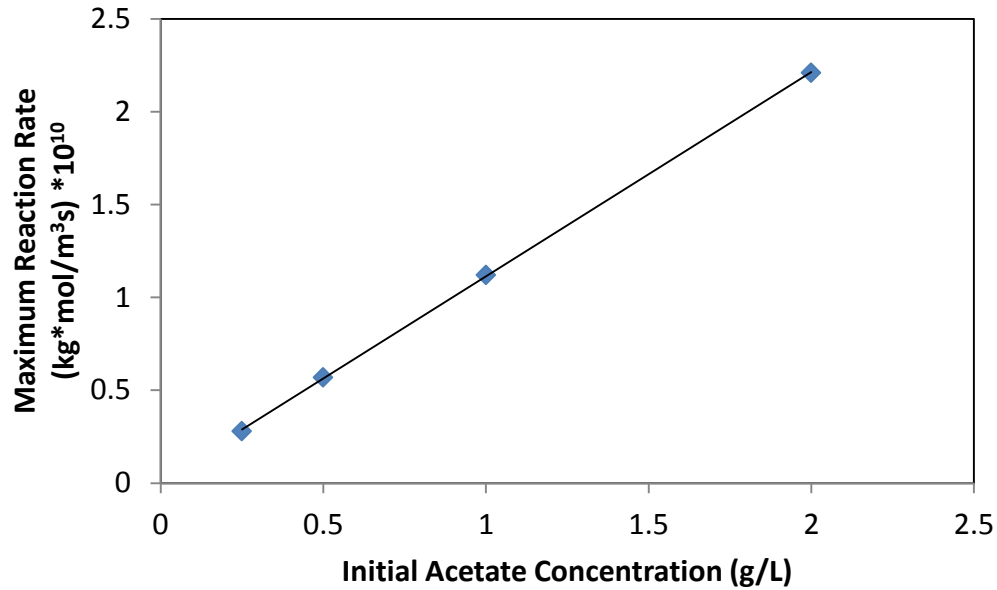
Figure 4.13: Relationship between initial acetate concentration and maximum reaction rate for 2D analysis.

4.4.4. Two Parameter Parametric Study

The parametric study continues by varying two parameters of interest. From the case studies presented, the most interesting combinations of parameters are simulated. All case studies will include 2D and 3D comparisons, and will include higher than base inlet velocities as it is clear that this parameter is the most influential on the flow. Inlet velocity is also very easily adjustable in experimental settings [32]. A summary of the new cases can be found in Table 4.2.

Table 4.2: Parametric study cases that vary multiple parameters.

Case	Inlet Velocity (m/s)	Acetate Concentration (g/L)	Temperature (K)
Base Case	0.00002	0.5	300
Case 10	0.002	1	300
Case 11	0.02	0.25	300
Case 12	0.0002	0.5	400

4.4.4.1. Case 10 – High Velocity, High Acetate Concentration

The case study explores the effects of a higher inlet velocity and high initial acetate concentration. Temperature is held at the base value (300 K) to allow for comparisons to other cases already presented. Figure 4.14 shows the 2D results, where high regions of acetate occur near the outlet, which is undesirable. This is a trend that is observed with other higher velocity cases (Figure 4.9 (c, d)); however, reaction rates are the highest of any case due to a high inlet velocity and increased concentration. Both sets of contours for this case are most visually similar to those with the same inlet velocity (Figure 4.14 (a, b) and (c, d)). Comparing the reaction rates at the inlet (Figure 4.14 (d)) to those of the identical case with half the concentration (Figure 4.14 (c)), the results showed that the linear relationship is upheld; the maximum reaction rate (1.19×10^{-9} kg·mol/(m^3·s)) is linearly related to that of the case with half the initial concentration (5.94×10^{-10} kg·mol/(m^3·s)). Case 10 also has a reaction rate that is an order of magnitude greater than Case 8 and the base case, thus both reaction rates for these cases appear to be entirely below the minimum value on the legend (Figure 4.14 (a, b)).
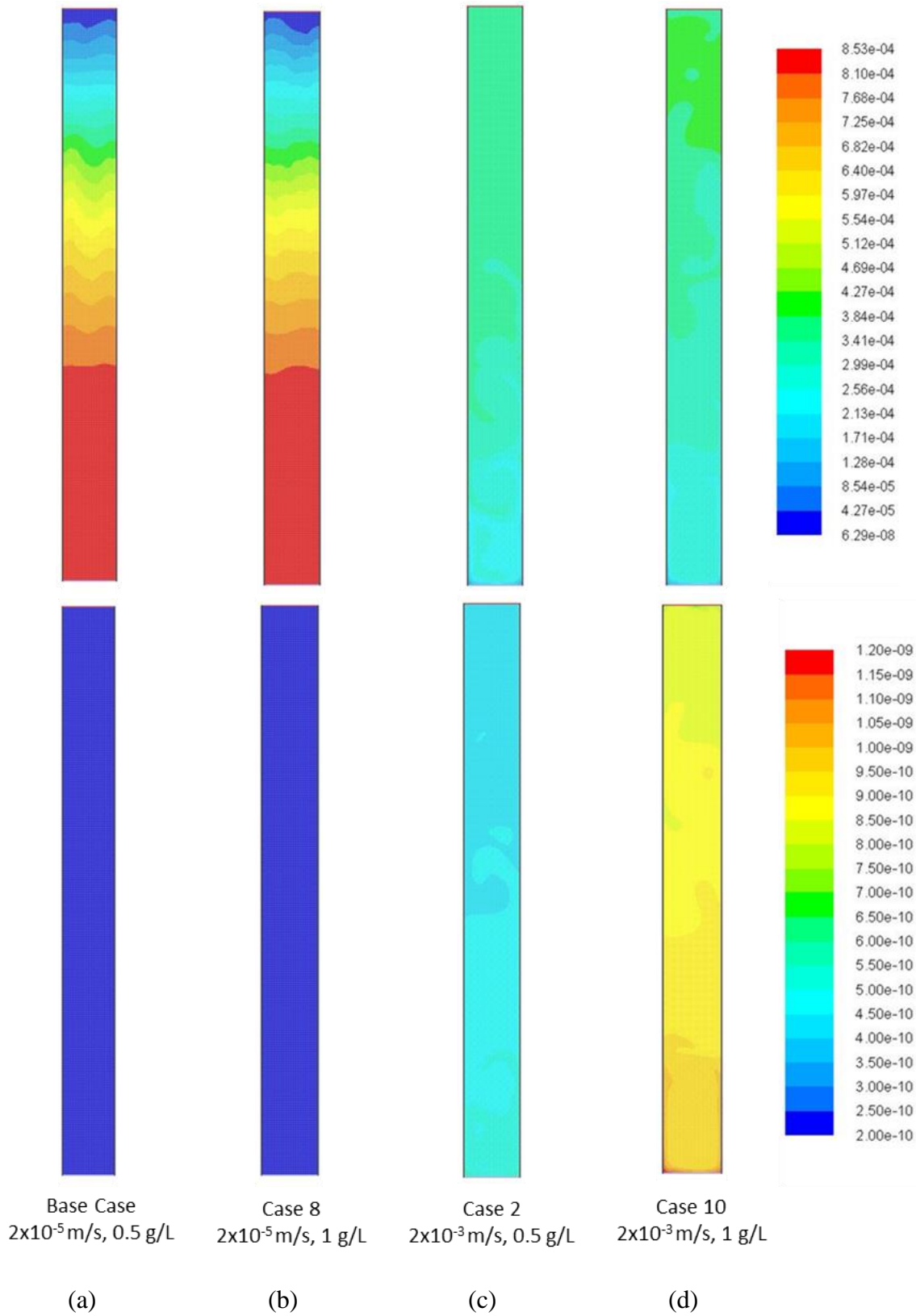
Figure 4.14: Contours of acetate molar concentration (top) in kmol/m^3 and reaction rate (bottom) in kg·mol/(m^3·s) to compare effects of velocity and concentration.

74

In Figure 4.15, the 3D results are compared to the 2D results shown previously. The 3D predictions for reactions occur at a higher rate, and 50% farther up the channel compared to the base case. This seems like it would be common sense that a higher inlet velocity would cause reactions to occur farther up the channel, but since the simulation time is based on hydraulic retention time, higher inlet velocities result in shorter simulated time. This allows for common ground to compare results, thus making the 50% increase in reaction space a substantial result. Also, the maximum concentration and reaction values for the case study were significantly greater than the base case. When comparing the 3D to the predictions, the reaction rates contours are directly applicable; however, the concentration contours have taken into account the adjusted range discussed in Section 4.3.2. The 2D acetate concentration predictions shown in Figure 4.15 (a-b) are the same data shown in Figure 4.14 (a, d), but with different minimum and maximum ranges for the legend. The most noticeable difference between the 2D and 3D cases is that both contours in 2D have more evenly distributed values throughout the chamber, while the 3D case has very concentrated regions of reactions and acetate concentration near the inlet only. Also, the maximum reaction rates between 2D and 3D Case 10 results are nearly identical, at 1.19×10^{-9} kg·mol/(m^3·s) (Figure 4.15 (b)) and 1.28×10^{-9} kg·mol/(m^3·s) (Figure 4.15 (d)), respectively.
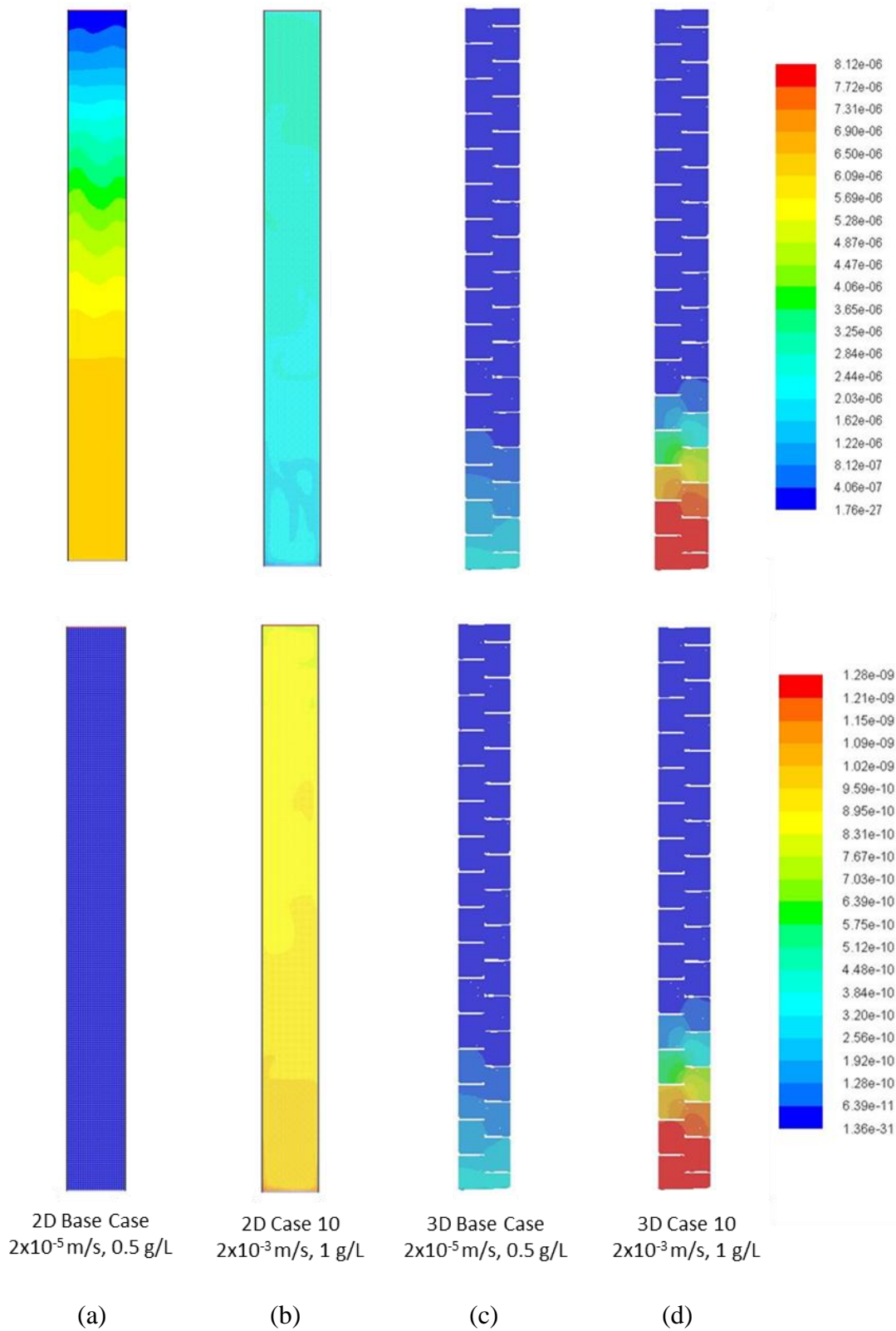
Figure 4.15: Contours of acetate molar concentration (top) in kmol/m^3 and reaction rate (bottom) in kg·mol/(m^3·s) to compare 2D and 3D results of Case 10 and the base case.

76

4.4.5. Case 11 – High Velocity, Low Concentration

Case 11 differs from case 1 as it uses a higher inlet velocity and a much lower acetate concentration. Temperature is once again held constant in order to allow for comparison to existing results. The 2D results again show high regions of acetate near the outlet. However, reaction rates are relatively high (Figure 4.16 (d)), though lower than Case 10 (Figure 4.14 (d)) because of a greatly reduced concentration of acetate. The cases with lower inlet velocities (Figure 4.16 (a, b)) looked more similar to each other, thus further supporting that inlet velocity is the dominant parameter of the three investigated. The linear hypothesized relationship between initial acetate concentration and maximum reaction rate is upheld again in Case 11. Case 3 (Figure 4.16 (c)) has twice the initial acetate concentration, and its maximum reaction rate of 6.40×10^{-10} kg·mol/(m^3·s) again agrees with the linear trend when compared to the maximum reaction rate of Case 11 (Figure 4.16 (d)), which is 3.20×10^{-10} kg·mol/(m^3·s). It is also interesting to observe that although the base case (Figure 4.16 (a)), has a higher acetate concentration, the reaction rate is still higher in Case 11 (Figure 4.16 (d)) because of the influence of the higher inlet velocity.
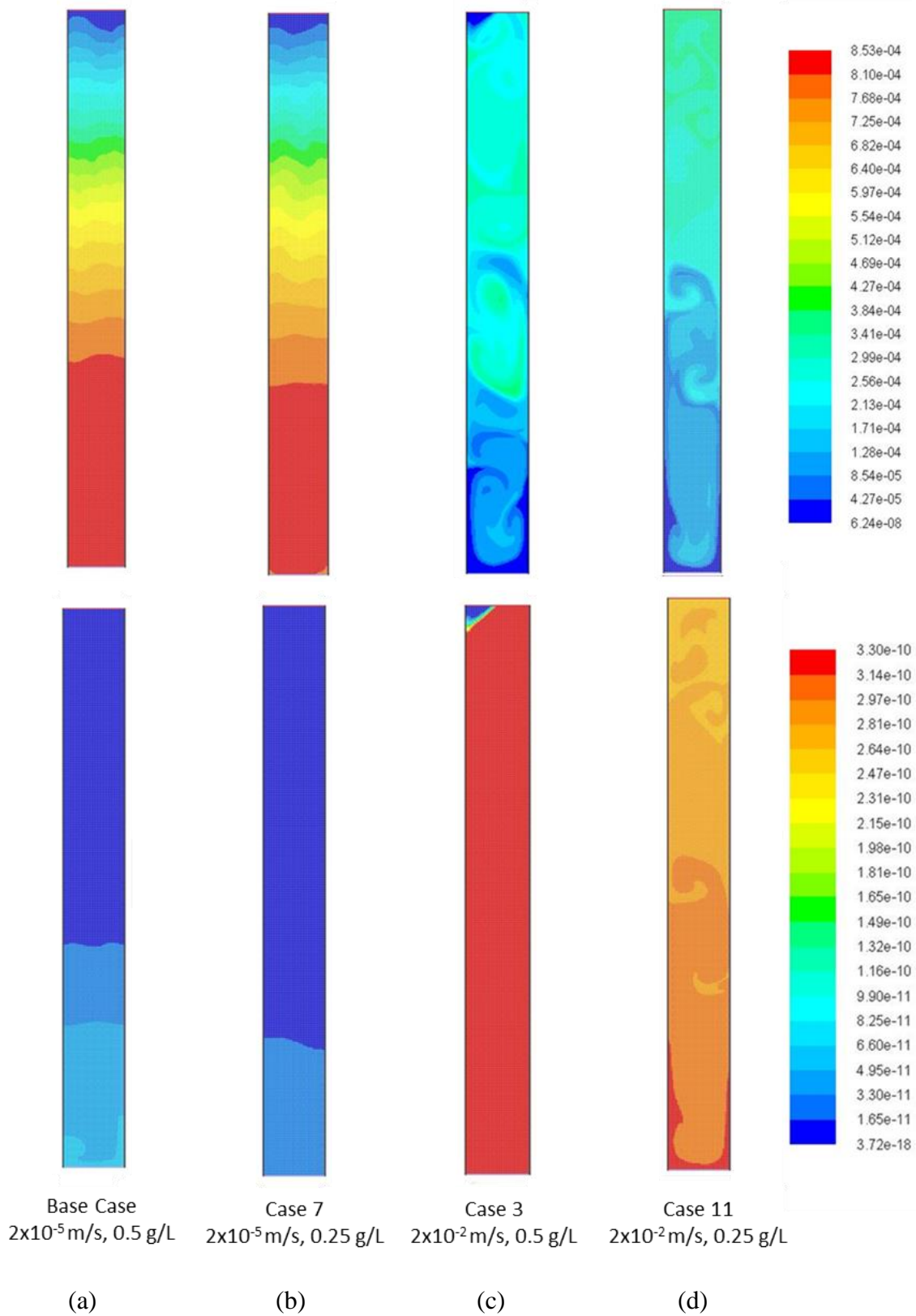
Figure 4.16: Contours of acetate molar concentration (top) in kmol/m^3 and reaction rate (bottom) in kg·mol/(m^3·s) to compare effects of velocity and concentration.
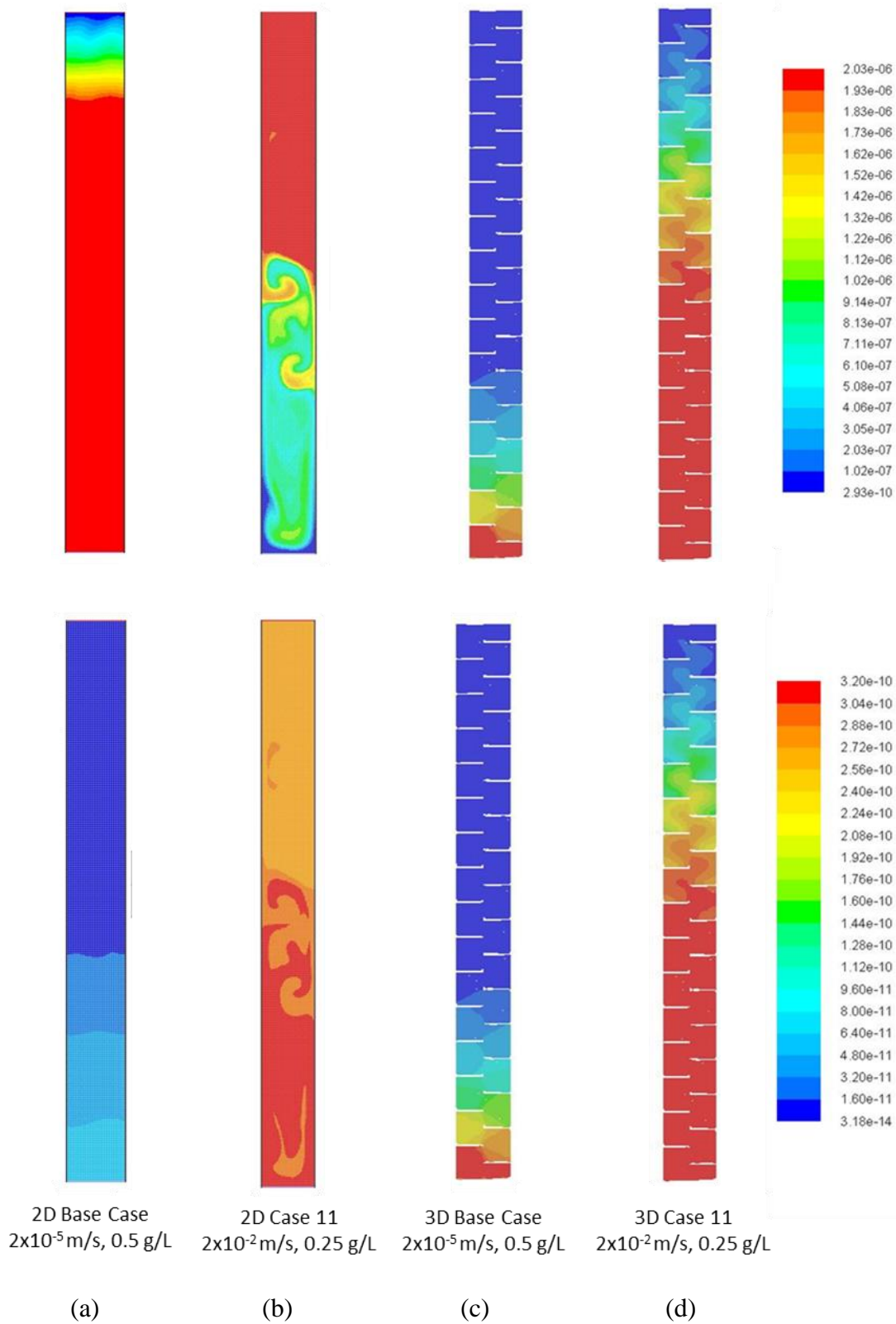
Figure 4.17: Contours of acetate molar concentration (top) in kmol/m^3 and reaction rate (bottom) in kg·mol/(m^3·s) to compare 2D and 3D results of Case 11 and the base case..

Figure 4.17 compares the 2D and 3D predictions for the base case and Case 11. In the 3D results (c-d), the most noticeable difference is how far up the channel reactions occur and acetate can be found. In Case 11 (Figure 4.17 (d)), reactions nearly reach the top of the channel, and occur over 2.5 times farther up the channel than the 3D base (Figure 4.17 (c)). This same trend can also be observed in the contours of acetate concentration. It is interesting to note that while the Case 11 reactions do not occur as far up the channel as the 3D base case, they do occur at higher maximum rates: 4.114 x 10^{-10} kg·mol/(m^3·s) for the base case compared to 3.199 x 10^{-10} kg·mol/(m^3·s) for Case 11. This maximum reaction rate is exactly the same for both the 2D and 3D Case 11 results, further supporting a trend that was observed in the Case 10 study. When comparing the 2D and 3D acetate concentrations, it is apparent that the trends are completely opposite; the 2D case has more acetate near the top of the chamber and the 3D case has more acetate near the bottom. This seems to support the hypothesis that the 3D geometry does not display the adverse effects of high inlet velocities that are evident in the 2D geometries (Figure 4.9). Also, the reaction rate in 2D Case 11 is much more evenly distributed than in 3D case 11. A reasonable explanation is that the spiral spacer disrupts the flow in the more complex, 3D geometry. It can also be clearly observed in 3D Case 11 that reactions occur at a higher rate closer to the center of the channel. While this could be observed slightly in the Case 10 study (Figure 4.15 (d)), it is much more evident that reaction rates are far more developed in Case 11. This information supports the claim to have the micro-organisms on the bristles concentrated closer to the center of the chamber, as it seems this is naturally the area of highest reaction density.

4.4.6. Case 12 – High Velocity, High Temperature

The purpose of Case 12 is to investigate the effects of both higher temperature and slightly higher inlet velocity. Case 12 holds acetate concentration constant to allow for comparisons between previous cases. The 2D results in Figure 4.18 again confirm that cases with the same inlet velocities (Figure 4.18 (a, b) and (c, d)) have the most similar acetate concentrations and reaction rates. This shows that not only is inlet velocity a more significant parameter than initial acetate concentration, which was supported by Cases 10 and 11, but it is also a more significant parameter than temperature. Acetate concentrations occur at more evenly distributed values throughout the channel in Case 12 (Figure 4.18 (d)). Also, the maximum acetate concentration is lower in Case 12 than in Case 1 (Figure 4.18 (c)), which is identical except with a lower temperature. This is expected, as it was discovered in the temperature study (Figure 4.11) that as temperature increases, maximum acetate concentration levels decrease. These results do not confirm or deny the conclusions made in the temperature study (Figure 4.10), but they do provide evidence for the fact that the relationship between temperature and maximum acetate concentration is a function of inlet velocity as well, since both Cases 1 and 12 have an inlet velocity an order of magnitude greater than the Cases 4-6 observed in the temperature study. The reaction rate contours only helped to confirm that temperature changes have very little effect on the chemical reaction occurring, as the pairs of cases with the same velocity and different temperatures (Figure 4.18 (a, b) and (c, d)) have nearly identical reaction rate contours.
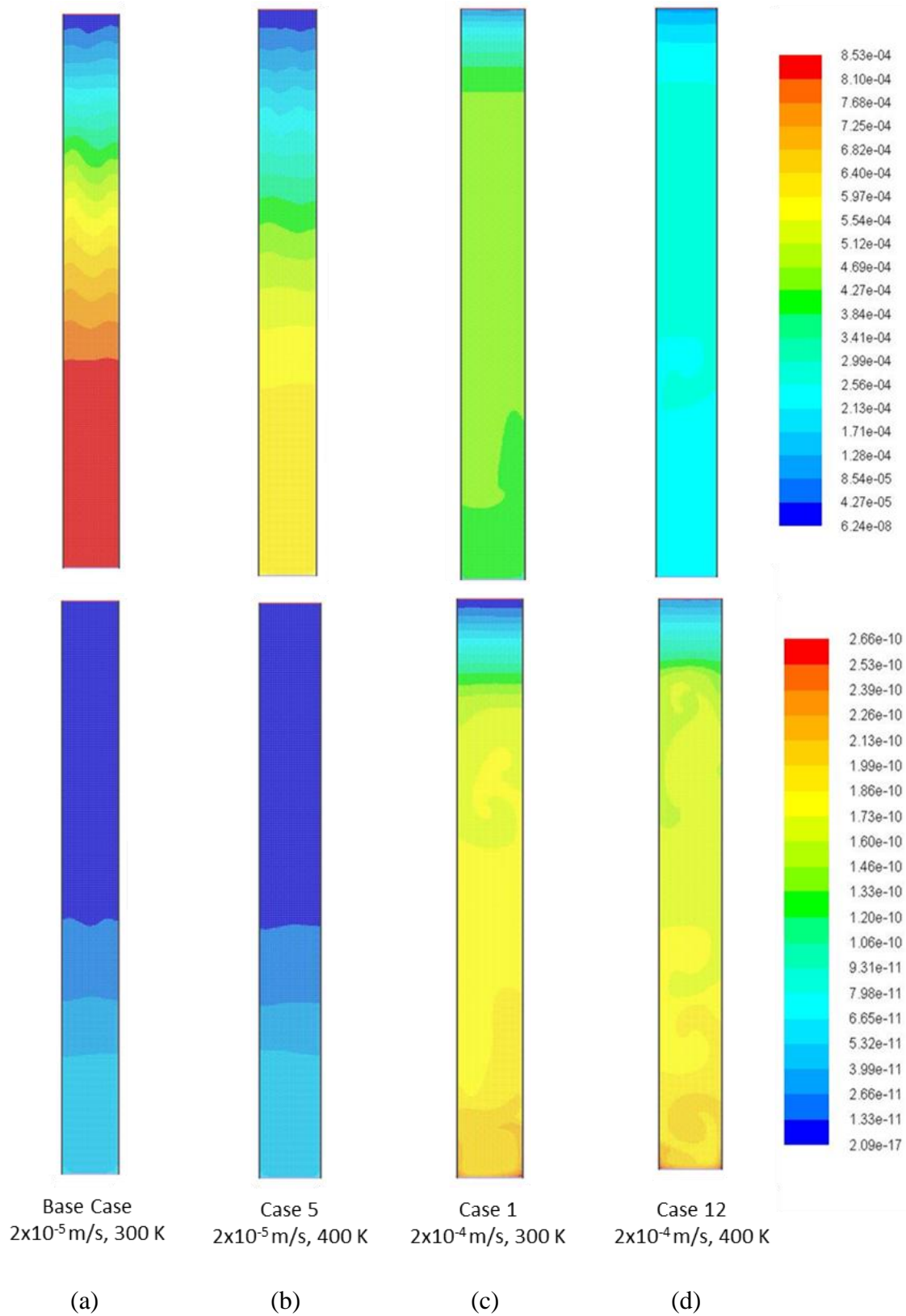
Figure 4.18: Contours of acetate molar concentration (top) in kmol/m^3 and reaction rate (bottom) in kg·mol/(m^3·s) to compare effects of velocity and temperature.

In Figure 4.19, the 3D Case 12 results are compared to the 2D Case 12 results. In the 3D results, the most noticeable difference is again how far up the channel reactions occur and acetate can be found. In 3D Case 12, reactions occur over twice as far up the channel than the 3D base case. A similar trend can be observed in the contours of acetate concentration. Not only do reactions occur over twice as far up the channel, but they also occur at higher maximum rates in Case 12 due to the higher inlet velocity. Case 12 is the first two parameter case study in which the reaction rates are not similar between the 2D and 3D cases (Figure 4.19 (b, d)). This may have something to do with the fact that the temperature is 400 K, instead of 300 K like Cases 10 and 11, though this has been shown not to be an important parameter in 2D studies (Figure 4.11). It is possible that the effect of temperature is more significant in 3D cases. When comparing the 2D and 3D contours, it is apparent that both the acetate concentrations and reaction rates in the 2D geometry (Figure 4.19 (b)) are much more evenly distributed than in the 3D geometry (Figure 4.19 (d)). This has been observed in all of the 2D to 3D comparisons and is a product of the geometrical differences between the cases.

Additional parameters were evaluated and the results of these studies can be found in Appendix B. To summarize the results of the MFC parameter study, it is clear that the most influential parameter of the three studied is inlet velocity. There is also a relationship between initial acetate concentration and maximum reaction rate, as well as a relationship between temperature and maximum acetate concentration. There are significant differences in the flow between 2D and 3D geometries, which are most likely caused by the presence of the spiral spacer.
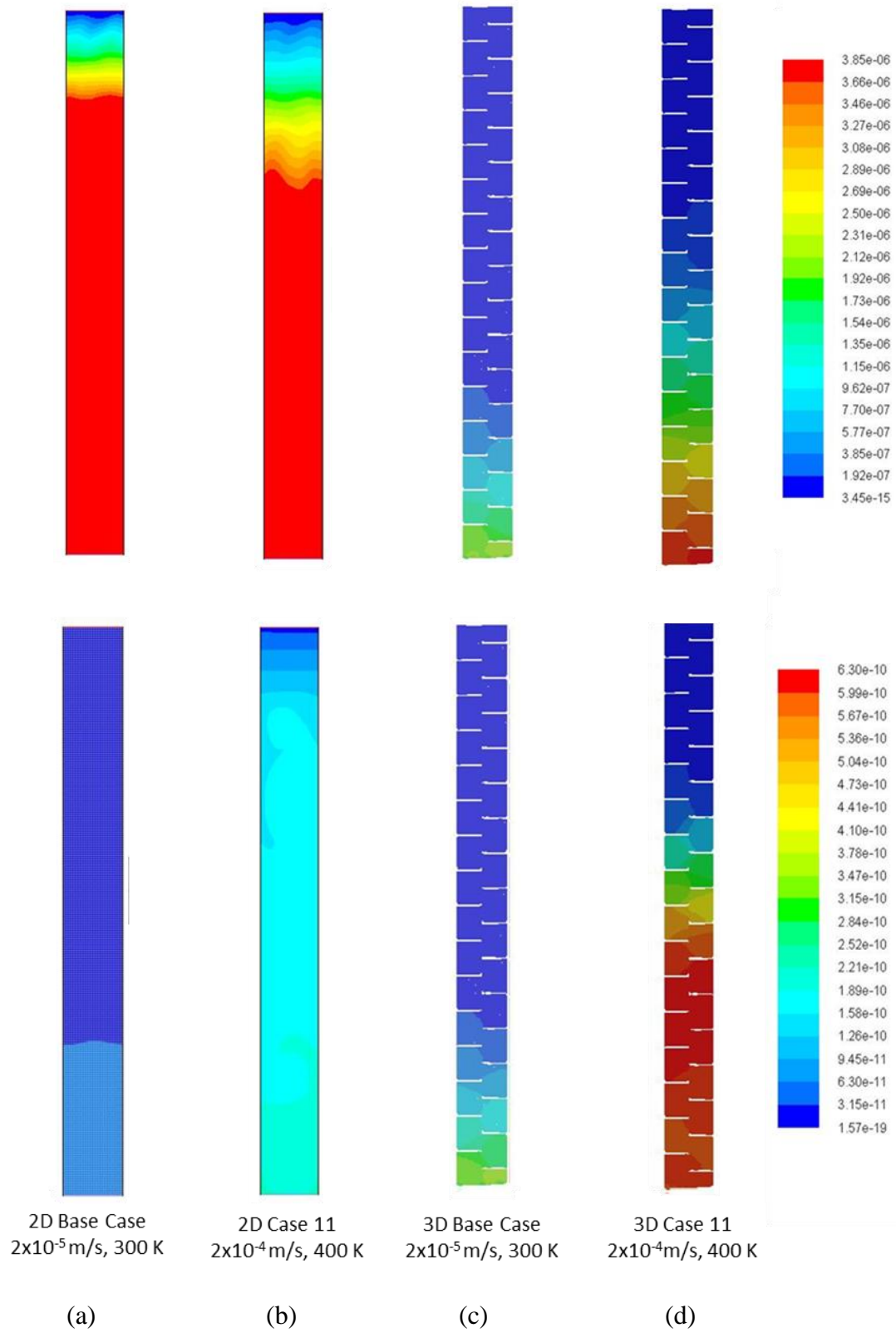
Figure 4.19: : Contours of acetate molar concentration (top) in kmol/m^3 and reaction rate (bottom) in kg·mol/(m^3·s) to compare 2D and 3D results of Case 12 and the base case..

Chapter 5. Conclusions

Through this study, not only was much learned about bubble columns and the interior flow of the reaction chamber of an MFC, but computational skills were developed that can hopefully be built upon by future researchers. This relationship between the experimental and computational realms of science is symbiotic, and it would be a great accomplishment to continue the multiphase flow and MFC projects to utilize that harmonious connection. The benefits that this work can provide may not be immediate, but they have the potential to improve the understanding of both two-phase flow and modeling MFCs which can impact many fields of study.

5.1.   Summary

The study that has been detailed in the previous sections is divided into two related, but separate sections. Before the results of either section were presented, the background and numerical models governing the CFD simulations were presented. This framed the work that followed and provided the impetus for the studies of both bubble columns and microbial fuel cells.

The bubble column study began with a substantial parametric study of a 2D model. This study used the experimental data and geometry described by Rampure et al. [8] to validate the predicted results and form the most accurate model to represent the physical system. In this process, a revised volume fraction discretization model was utilized to help correct non-physical results that occurred when using an updated version of Fluent to simulate cases. During a comprehensive grid resolution study that included the calculation of the GCI, an interesting relationship between the bubble diameter, d_b, and cell size, Δ, was discovered whereby, their ratio should ideally be $1/\sqrt{2}$ for the most accurate predictions. This relationship was confirmed

and explained the interesting results that fine grid resolutions predicted in the 2D bubble column simulations.

The parameters that were determined to be most appropriate for modeling the two-phase flow of a bubble column are summarized here. Simulations do not employ virtual mass, neglect drift and surface tension, use the Schiller-Naumann drag model, the dispersed $k - \varepsilon$ turbulence model with no turbulence specified at the boundaries, and simulate a bubble diameter of 0.005 m. In addition, the Green-Gauss node based spatial discretization and modified HRIC volume fraction discretization are employed, using a 30x300 grid resolution, and implicit, first-order time discretization. Finally, a time-step of 0.005 seconds was used, with 100 time-samples per second for time averaging and 50 iterations per time-step, and all residuals are required to converge to 10^{-4}.

A 3D bubble column study was also performed. This study included a spatial averaging analysis that supported the conclusion that only two planes are necessary to fully capture the details of the flow. Also, a grid resolution and GCI study aided in the determination that 3D bubble column simulations to not struggle with the adverse effects of finer meshes that were observed in the 2D study. While 3D cases can be very accurate, the lengthy computational time for individual cases can make such simulations prohibitive, further supporting the importance of accurate 2D models.

Finally, a preliminary study of MFCs was presented. This study began with the explanation of the complex modeling required to capture the finer details of the MFC geometry. The chemical reactions that drive the MFC were then explained, and the first results using this new model were shown. A parameter study that evaluated the effects of inlet velocity, acetate

concentration, and temperature in both 2D and 3D geometries were then described. The conclusion of this study is that inlet velocity is the most influential of the three tested parameters, and that there are substantial differences between the 2D and 3D geometries. The 3D results appeared to be the most physical, but they were also the most computationally expensive. There is more work to be done on this study, but the results presented provide a strong beginning to an interesting problem.

5.2. Future Work

Beyond what was achieved in this study, there is still a tremendous amount to be learned and discovered. With respect to the MFC work, the first modification to the geometry that would greatly improve the system would be to model the bristles within the chamber. These would most likely be a semi-porous region of the chamber in which the reaction takes place. In addition, the entire fuel cell system could be modeled, which would provide more realistic conditions up- and downstream of the chamber. This would also allow for additional parameters to be controlled as they would be in actual operation of the fuel cell. The chemical reaction could be more sophisticated than it currently is. Instead of having a one-step reaction, there are many sub-reactions that could be modeled that would provide a more accurate representation of the actual occurrence of reactions within the chamber.

Adjusting parameters within the chemical reaction study may also improve the convergence, as certain cases did not converge to levels desired in most CFD cases. While tedious and time consuming, this would be a valuable addition to the current body of work. Specifically, a comprehensive turbulence model study could be performed in 3D cases as this is expected to have a significant impact on the flow characteristics for cases with higher inlet velocities. Other studies in the Crest laboratory have explored the use of the realizable $k - \varepsilon$

model in the presence of chemical reactions, although turbulence models do not display true effects until run in 3D cases. Some preliminary parameter tests were explored in the Appendix, but more work will need to be done to have confidence in the results. The system model also needs to be validated by experimental data. A paper provided by the civil engineering team introduces data that could be used to adjust the model and test its reliability [32]. In this study, a slightly larger geometry is used, compared to the geometry currently in the lab, which was used as the basis for these cases. Also, due to the larger size, larger inlet velocities will need to be tested, although all of the recommended inlet velocities are within the range explored in this study. The data is presented in terms of current density and removal of chemical oxygen demand. While neither of these values are tracked in Fluent simulations, comparisons can be made between reaction rates, species concentrations, and possibly other unexplored parameters.

For work on the bubble column study, there is much to be explored in the 3D realm. While a robust parameter study was performed in 2-dimensions, some of these same parameters were not explored in as much detail for 3D geometries. Also, the meshing technique, while sufficient, was not optimized. Working to find the most efficient meshing scheme for cylindrical columns could be very valuable, and may reduce some of the issues encountered in this study.

References

[1] Cha, J., Choi, S., Yu, H., Kim, H., and Kim, C., 2010. *Directly Applicable Microbial Fuel Cells in Aeration Tank for Wastewater Treatment.* Bioelectrochemistry 78 (2010) 72-79.

[2] He, Z., 2013. *Microbial Fuel Cells: Now Let Us Talk About Energy*. Environmental Science & Technology 47 (2013) 332-333.

[3] Tarasevich, S., Giniyatullin, A., 2012. *Verification and Validation of Heat Transfer and Friction Factor in Tubes with Various Twisted Tape Inserts at One Phase Flow*. Proceedings of The ASME 2012 Verification & Validation Symposium.

[4] Spicka, P., Dias, M. M., and Lopes, J. C. B., 2001. *Gas-liquid Flow in a 2D Column: Comparison Between Experimental Data and CFD Modelling*. Chemical Engineering Science Vol 56, Iss 21-22 (2001) 6367-6383.

[5] Diaz, E. M., Montes, F. J., and Galan, M. A., 2009. *Influence of the Lift Force Closures on the Numerical Simulation of Bubble Plumes in a Rectangular Bubble Column*. Chemical Engineering Science Vol. 64, Iss 5 (2009) 930-944.

[6] Law, D., Battaglia, F., and Heindel, T. J., 2008. Model validation for low and high superficial gas velocity bubble column flows. Chemical Engineering Science 63 (2008) 4605-4616.

[7] Law, Deify, 2010. *Computational Modeling and Simulations of Hydrodynamics for Air-Water External Loop Airlift Reactors*. Ph.D Thesis, Virginia Polytechnic Institute and State University.

[8] Rampure, R.M., Buwa, V.V., and Ranade, V.V., 2003. *Modeling of gas–liquid/gas–liquid–solid flows in bubble columns: experiments and CFD simulations*. The Canadian Journal of Chemical Engineering 81, 692–706.

[9] Mudde, R.F., Lee, D.J., Reese, J., and Fan, L.-S., 1997. *Role of coherent structures on Reynolds stresses in a 2-D bubble column*. A.I.Ch.E. Journal 43, 913–926.

[10] Celik, I. B., Ghia, U., Roache, P., and Freitas, C., 2008. *Procedure for Estimation and Reporting of Uncertainty Due to Discretization in CFD Applications*. Journal of fluids Engineering-Transactions of the ASME, Vol. 130, No. 7.

[11] Lage, P.L.C., and Espósito, R.O., 1998. *Experimental determination of bubble size distributions in bubble columns: prediction of mean bubble diameter and gas hold up*. Powder Technology 101 (1999). 142-150

[12] Guenther C, Syamlal M, Longanbach J, and Smith P, "CFD modeling of a transport gasifier Part II", Proceedings of the 20th Annual Pittsburgh Coal Conference, Pittsburgh, PA, September 15-19, 2003

[13] Coroneo, M. *CFD prediction of segregating fluidized bidisperse mixtures of particles differing in size and density in gas-solid fluidized beds*. Chemical Engineering Science 66 (2011) 2317-2327.

[14] Monahan, S. M., Vitankar, V. S., and Fox, R. O., 2005. *CFD predictions for flow-regime transitions in bubble columns.* AIChE, Vol. 51, Issue 7. 1897-1923.

[15] Studley, Allison F., 2010. *Numerical Modeling of Air-Water Flows in Bubble Columns and Airlift Reactors*. Masters Thesis, Virginia Polytechnic Institute and State University.

[16] Logan, B. E., Hamelers, B., Rozendal, R., Schroder, U., Keller, J., Freguia, S., Aelterman, P., Verstraete, W., and Rabaey, K., 2006. *Microbial Fuel Cells: Methodology and Technology.* Environmental Science & Technology / Vol. 40, No. 17, 5181-5192.

[17] Picioreanu, C., van Loosdrecht, M., Curtis, T., and Scott, K., 2009. *Model based evaluation of the effect of pH and electrode geometry on microbial fuel cell performance.* Bioelectrochemistry 78 (2010) 8–24.

[18] Ge, Z., Zhang, F., Grimaud, J., Hurst, J., and He, Zhen, 2013. *Long-term investigation of microbial fuel cells treating primary sludge or digested sludge*. Bioresource Technology 136 (2013) 509–514.

[19] ANSYS, Inc, 2013, *ANSYS FLUENT 14.5 Theory Guide*.

[20] ANSYS, Inc, 2013, *ANSYS FLUENT 14.5 User Guide*.

[21] Panton, R., 2013. *Incompressible Flow*. John Wiley & Sons, Inc., Hoboken, NJ.

[22] Rafique, M., and Dudukovic, M. P., 2006. *Influence of Different Closures on the Hydrodynamics of Bubble Column Flows*. Chemical Engineering Communications, 193:1,1-23.

[23] Shah, Y. and Deckwer, W., 1983, "Hydrodynamics of bubble columns," *Handbook of Fluids in Motion,* Ann Arbor Science, pp. 583–620.

[24] Anderson, J.D., 1995. *Computational Fluid Dynamics: The Basics with Applications*. McGraw-Hill.

[25] Mahgerefteh, H., Rykov, Y., and Denton, G., 2009. *Courant, Friedrichs and Lewy (CFL) impact on numerical convergence of highly transient flows*. Chemical Engineering Science 64 (2009) 4969-4975.

[26] Arends, J., and Verstraete, W., 2012. *100 years of Microbial Electricity Production: Three Concepts for the Future.* Microbial Biotechnology 5 (2012) 333-346.

[27] Gerhartz, W. (exec ed.). *Ullmann's Encyclopedia of Industrial Chemistry*. 5th ed.Vol A1: Deerfield Beach, FL: VCH Publishers, 1985 to Present., p. VA24: 315

[28] Linstrom, P.J.; Mallard, W.G. (eds.) *NIST Chemistry WebBook, NIST Standard Reference Database Number 69*. National Institute of Standards and Technology, Gaithersburg MD. http://webbook.nist.gov (retrieved 2014-05-25)

[29] Lide, D.R. (ed.). *CRC Handbook of Chemistry and Physics*. 86th Edition 2005-2006. CRC Press, Taylor & Francis, Boca Raton, FL, p. 4-87.

[30] Zielinksi, M, 1983. *Oxidation of Sodium Acetate with Alkaline Permanganate*. Journal of Radioanalytical Chemistry, Vol. 80, Nos 1-2 (1983) 237-246.

[31] Moon, H., Chang, I. S., Jang, J. K., and Kim, B. H., 2005. *Residence time distribution in microbial fuel cell and its influence on COD removal with electricity generation*. Biochemical Engineering Journal 27 (2005) 59–65.

[32] Zhang, F., Ge, Z., Grimaud, J., Hurst, J., and He, Z., 2013. *Improving electricity production in tubular microbial fuel cells through optimizing the anolyte flow with spiral spacers*. Bioresource Technology 134 (2013) 251-256.

Appendix A

Table A.1: Chemical Compound Data

Compound	Chemical Formula	Density (g/cm^3)	Specific Heat (J/(mol·K))	Molecular Weight (g/mol)
Sodium Acetate	$NaCH_3COO$	1.528	100.83	82.030
Sodium Bicarbonate	$NaCH_3COO$	2.200	1.047	84.007
Sodium	Na	0.927	1.23	22.990

Appendix B

B.1.   *Turbulence Model Study*

As was explored in the bubble column study, the turbulence model needs to be examined to determine what is most appropriate for this case. The cases shown previously were all run with the default laminar settings due to low inlet velocities. The bubble column study employed the use of the $k - \varepsilon$ model, and the realizable $k - \varepsilon$ model is also investigated. This model is selected since other studies in the CREST laboratory have run chemical reaction simulations and the realizable $k - \varepsilon$ model was determined to be most suitable for those applications. While the standard $k - \varepsilon$ model is most appropriate for bubble column applications, there is enough difference in the MFC case to expect it is likely not the ideal model. This study is only performed in 2D, and is not sufficient to confirm which model is best. In order to truly capture the turbulence in a system, it must be simulated in 3D. Therefore, these results may be interesting, but are not strong enough to make definitive conclusions about the appropriate turbulence model for this system.

The results of this study shown in Figure B.1 demonstrate that introducing a turbulence model to the flow makes a significant effect on both acetate concentration and reaction rate. There is nearly no difference in these cases between the realizable and standard $k - \varepsilon$ models (Figure B.1). Both have lower reaction rates and thus higher acetate concentrations than the laminar case. This provides information that a turbulence model does affect the flow, but it must be explored in 3D cases to ascertain just how significant this impact is.
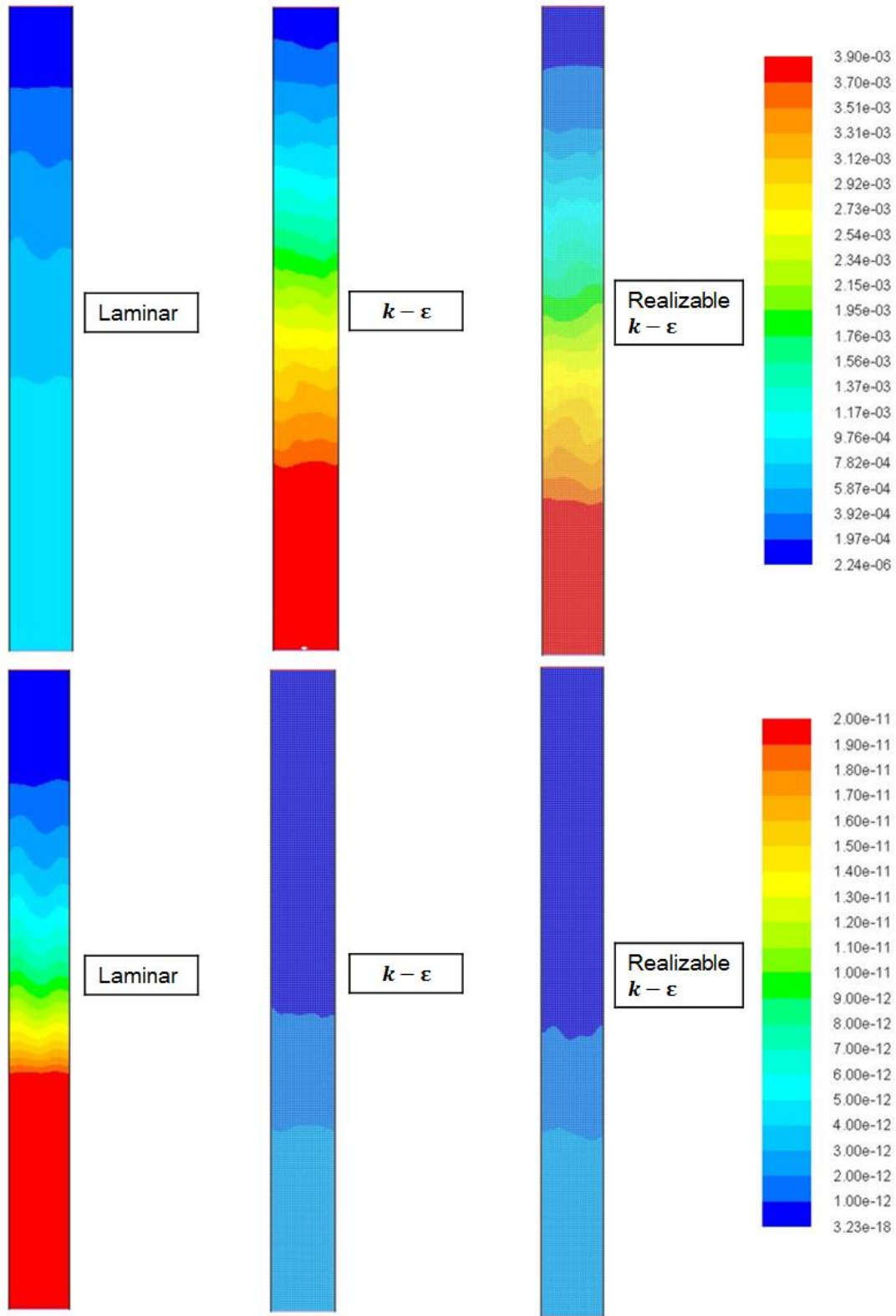
Figure B.1: Contours of acetate molar concentration (top) in kmol/m^3 and reaction rate (bottom) in kg·mol/(m^3·s) to compare different turbulence models.

B.2. *Discretization Schemes*

In this section, both the spatial and gradient discretization schemes are compared. The cases shown earlier were all run with the first order upwind spatial discretization and a least-squares cell-based gradient discretization. The QUICK spatial discretization and Green-Gauss node based gradient discretization schemes, which were used in the bubble column study, are compared to the least-squares cell-based scheme.

The results in the Figure B.2 show that the discretization schemes do not make a tremendous impact on the flow conditions in the 2D geometry. While the acetate concentrations in the case using the QUICK spatial discretization scheme are noticeably higher than the other cases, the actual differences between the cases are likely negligible. The reaction rate contours are also nearly identical, which further supports that the discretization schemes do not make significant impacts on the flow characteristics in these cases.
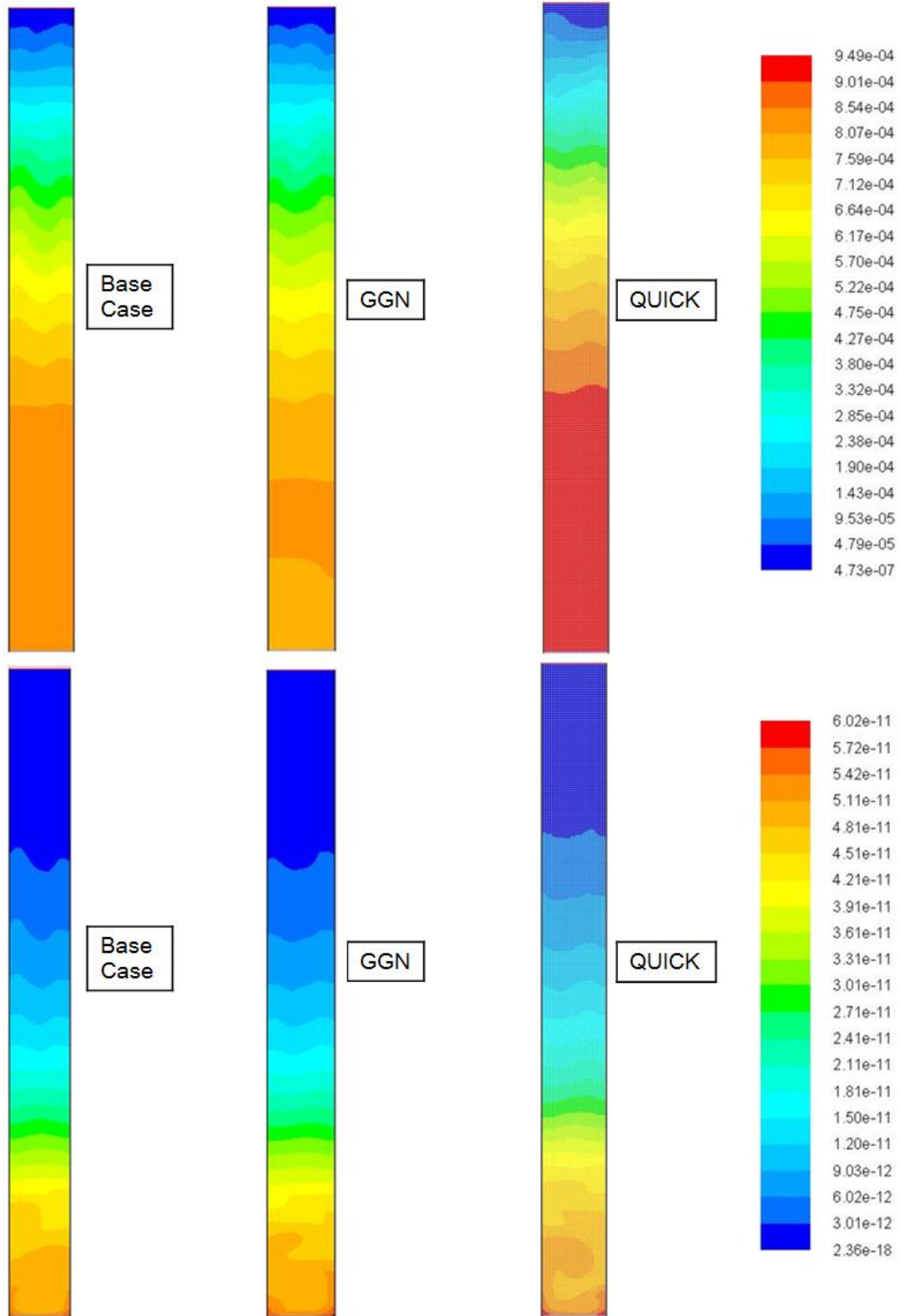
Figure B.2: Contours of acetate molar concentration (top) in kmol/m^3 and reaction rate (bottom) in kg·mol/(m^3·s) to compare discretization schemes.

B.3.   *3D Contour Study*

As can be observed in almost every 3D MFC case presented in Chapter 4, the contours between both the reaction rates and acetate concentration appear to have identical patterns. While the units and legends are different, the two contours are otherwise indistinguishable. The explanation for why this is the case in the 3D results and not in the 2D cases is linked to a question that came up previously. The 2D cases consistently have acetate concentrations that are orders of magnitude greater than the 3D results. This is a product of the differing geometries, and while comparisons can be made, these values do affect the reactions. It is obvious that without the presence of acetate, no reactions can occur; however, if all the acetate in the system is consumed before the system is saturated there is an interesting effect. Reactions will occur at a rate directly proportional to the acetate concentration unless there is an excess of acetate in the system. Because of the low acetate concentrations in the 3D cases, the correlation occurs and the contours seem to be exactly the same. Since the simulations in 2D has seemingly higher acetate concentrations, not all of the acetate was reacting, and the excess causes regions where there is no longer a proportional rate of acetate concentration to reactions. To confirm this, a case was run in a 3D geometry with an initial acetate concentration of 100 g/L. This concentration is 200 times the base case value, and thus makes the simulated acetate concentrations similar to those of the 2D cases.   The results, displayed in Figure B.3, show that increasing the acetate does cause the contours of acetate concentration and reaction rate to differ substantially. This supports the claim that with the low concentrations, the only reason the two contours appear the same is that all the acetate is reacting, causing a direct correlations between reactions and acetate levels.
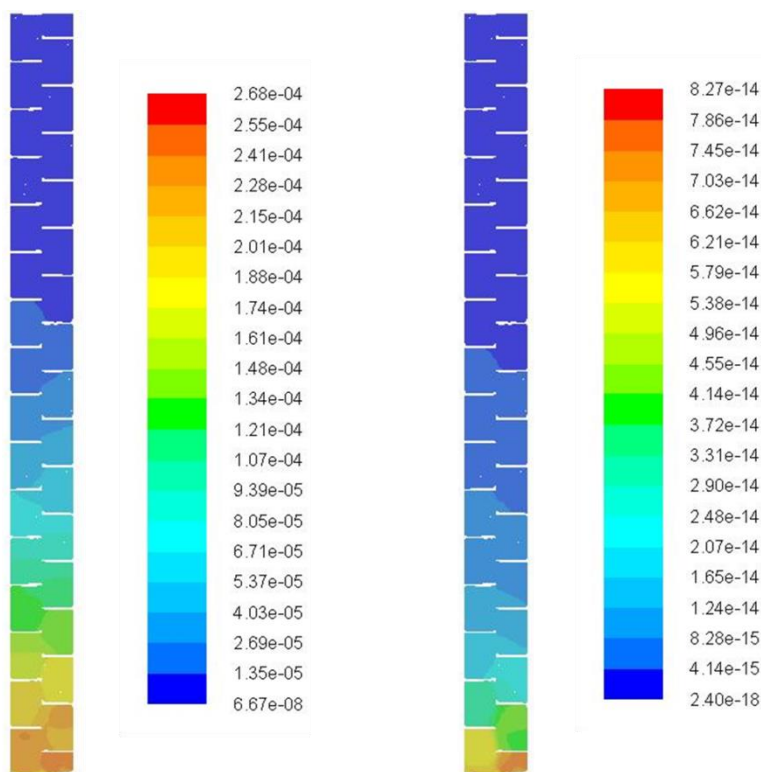
Figure B.3: Contours of acetate molar concentration (left) in kmol/m^3 and reaction rate (right) in kg·mol/(m^3·s) to compare effects of high acetate concentrations.

B.4.   2D to 3D Comparison

An empty 3D column is also simulated with chemical reactions and the results can be observed in this section. While there are similarities between these results and both the 2D and 3D MFC cases, there are more differences. The results, shown in Figure B.4 do not resemble any of the patterns of the 2D cases, and the easiest explanation is that the change in geometry from 2D to 3D made a significant impact on the results. The spacer in the MFC could explain many of these differences as well, but there are no definitive results that can be determined from this comparison. It is interesting to note that the reaction rates between the 2D and 3D empty channel cases occur approximately the same distance up the channel. There are no noticeable relationships between the 3D empty channel and the 3D MFC cases or the 2D and 3D empty channel acetate concentration contours.
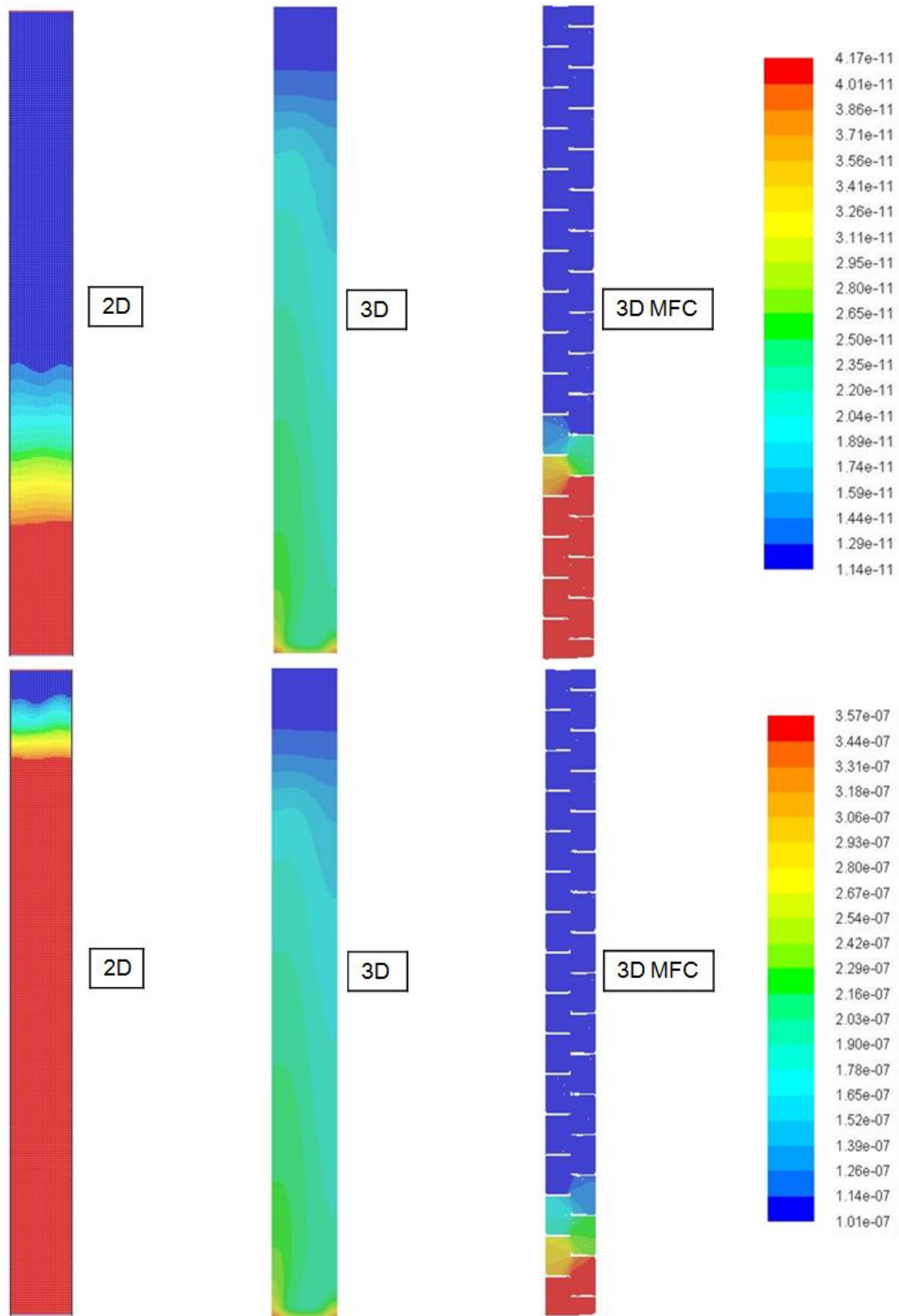
Figure B.4: Contours of acetate molar of acetate (top) in kmol/m^3 and reaction rate (bottom) in kg·mol/(m^3·s) to compare different geometries.